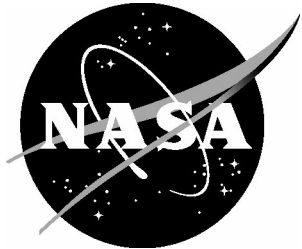


NASA/TM-20210013648



# High-Fidelity Simulation of Turbulent Flow Past a Gaussian Bump

*Ali Uzun and Mujeeb R. Malik  
Langley Research Center, Hampton, Virginia*

## NASA STI Program Report Series

Since its founding, NASA has been dedicated to the advancement of aeronautics and space science. The NASA scientific and technical information (STI) program plays a key part in helping NASA maintain this important role.

The NASA STI program operates under the auspices of the Agency Chief Information Officer. It collects, organizes, provides for archiving, and disseminates NASA's STI. The NASA STI program provides access to the NTRS Registered and its public interface, the NASA Technical Reports Server, thus providing one of the largest collections of aeronautical and space science STI in the world. Results are published in both non-NASA channels and by NASA in the NASA STI Report Series, which includes the following report types:

- **TECHNICAL PUBLICATION.** Reports of completed research or a major significant phase of research that present the results of NASA Programs and include extensive data or theoretical analysis. Includes compilations of significant scientific and technical data and information deemed to be of continuing reference value. NASA counterpart of peer-reviewed formal professional papers but has less stringent limitations on manuscript length and extent of graphic presentations.
- **TECHNICAL MEMORANDUM.** Scientific and technical findings that are preliminary or of specialized interest, e.g., quick release reports, working papers, and bibliographies that contain minimal annotation. Does not contain extensive analysis.
- **CONTRACTOR REPORT.** Scientific and technical findings by NASA-sponsored contractors and grantees.

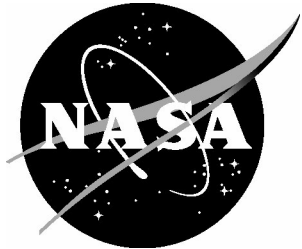
- **CONFERENCE PUBLICATION.** Collected papers from scientific and technical conferences, symposia, seminars, or other meetings sponsored or co-sponsored by NASA.
- **SPECIAL PUBLICATION.** Scientific, technical, or historical information from NASA programs, projects, and missions, often concerned with subjects having substantial public interest.
- **TECHNICAL TRANSLATION.** English-language translations of foreign scientific and technical material pertinent to NASA's mission.

Specialized services also include organizing and publishing research results, distributing specialized research announcements and feeds, providing information desk and personal search support, and enabling data exchange services.

For more information about the NASA STI program, see the following:

- Access the NASA STI program home page at <http://www.sti.nasa.gov>
- Help desk contact information:  
<https://www.sti.nasa.gov/sti-contact-form/> and select the "General" help request type.

NASA/TM-20210013648



# High-Fidelity Simulation of Turbulent Flow Past a Gaussian Bump

*Ali Uzun and Mujeeb R. Malik*  
*Langley Research Center, Hampton, Virginia*

National Aeronautics and  
Space Administration

Langley Research Center  
Hampton, Virginia 23681-2199

---

May 2021

The use of trademarks or names of manufacturers in this report is for accurate reporting and does not constitute an official endorsement, either expressed or implied, of such products or manufacturers by the National Aeronautics and Space Administration.

Available from:

NASA STI Program / Mail Stop 148  
NASA Langley Research Center  
Hampton, VA 23681-2199  
Fax: 757-864-6500

# High-Fidelity Simulation of Turbulent Flow Past a Gaussian Bump

Ali Uzun

*National Institute of Aerospace, Hampton, Virginia 23666*

Mujeeb R. Malik

*NASA Langley Research Center, Hampton, Virginia 23681*

## Abstract

A spanwise-periodic computation of a turbulent flow past a Gaussian bump is performed in the form of a hybrid direct numerical simulation and wall-resolved large-eddy simulation. A fourth-order spatially-accurate flow solver is employed to perform the simulation, using 10.2 billion grid points for a Reynolds number of 170000 based on the bump height. The key findings from the simulation are reported in the acceleration and deceleration flow regions associated with the bump shape. Significant anisotropy in the normal Reynolds stresses, along both the wall-normal and streamwise directions, is observed within the acceleration region. The ratio between the Reynolds shear stress and turbulent kinetic energy in that region also experiences significant deviations from the norms of a zero pressure gradient turbulent boundary layer. The chosen Reynolds number generates strong flow separation in the adverse pressure gradient region, which is in contrast with a previous simulation at half the Reynolds number that only indicated incipient separation. An internal layer generated in the acceleration region evolves into a free shear layer that develops in the deceleration region and separates. Proper modeling of this inner layer appears crucial to predict the flow separation. Surface curvature effects on the attached flow development are also discussed.

## Nomenclature

|          |  |
|----------|--|
| $C$      | = logarithmic layer intercept constant   |
| $C_f$    | = time- and spanwise-averaged skin-friction coefficient                        |
| $C_f^z$  | = time-averaged skin-friction coefficient at a given spanwise location         |
| $C_p$    | = mean surface pressure coefficient  |
| $h$      | = speed bump height  |
| $k$      | = turbulent kinetic energy   |
| $K$      | = relaminarization parameter   |
| $L$      | = width of the experimental speed bump model                                   |
| $n$      | = wall-normal distance   |
| $N$      | = number of spanwise grid points   |
| $p$      | = pressure   |
| $R$      | = surface radius of curvature  |
| $Re_L$   | = Reynolds number based on $L$ , $\rho_\infty u_\infty L / \mu_\infty$         |
| $s$      | = surface distance   |
| $u$      | = streamwise velocity component in the local orthogonal coordinate system      |
| $u_\tau$ | = wall friction velocity   |
| $U$      | = mean streamwise velocity component in the local orthogonal coordinate system |
| $v$      | = wall-normal velocity component in the local orthogonal coordinate system     |
| $w$      | = spanwise velocity component  |

|                   |   |  |
|-------------------|---|--|
| $x$               | = | axial direction                                    |
| $y$               | = | vertical direction                                 |
| $z$               | = | spanwise direction                                 |
| $\alpha_f$        | = | filtering parameter                                |
| $\delta$          | = | boundary-layer thickness                           |
| $\delta_i$        | = | internal layer thickness                           |
| $\Delta_p$        | = | acceleration parameter                             |
| $\Delta n$        | = | grid spacing along the local wall-normal direction |
| $\Delta s$        | = | grid spacing along the local streamwise direction  |
| $\Delta z$        | = | spanwise grid spacing                              |
| $\kappa$          | = | von Kármán constant                                |
| $\mu$             | = | molecular viscosity                                |
| $\nu$             | = | kinematic viscosity, $\mu/\rho$                    |
| $\Psi$            | = | stream function                                    |
| $\rho$            | = | fluid density                                      |
| $\sigma$          | = | standard deviation                                 |
| $\Sigma$          | = | series summation                                   |
| $\tau_w$          | = | wall shear stress                                  |
| $\langle \rangle$ | = | temporal and spanwise averaging operator           |

#### *Subscripts*

|          |   |                                |
|----------|---|--------------------------------|
| $e$      | = | boundary-layer edge value      |
| $\infty$ | = | freestream value               |
| $\theta$ | = | momentum-thickness based value |

#### *Superscripts*

|     |   |                                    |
|-----|---|------------------------------------|
| $z$ | = | value at a given spanwise location |
| $'$ | = | perturbation from mean value       |
| $+$ | = | value in wall units                |

## 1 Introduction

The challenges associated with the satisfactory prediction of high Reynolds number turbulent flows simultaneously subjected to strong pressure gradient and surface curvature effects at an affordable computational cost have recently motivated the fluid dynamics community to embark on a new benchmark test case referred to as the “speed bump” flow [1]. This problem investigates the interaction of an incoming turbulent boundary layer with the strong favorable and adverse pressure gradients generated by a Gaussian bump, depicted in Figure 1, as the flow passes over it. Surface curvature effects present in the problem bring additional complications. The Reynolds number of the problem, based on the width of the experimental model,  $L$ , varies from about 1.3 million up to 3.5 million. A detailed experimental investigation is currently underway in the United States for this test case to generate new validation data for smooth body flow separation. Williams et al. [2], [3] recently reported the results from a different preliminary experiment for the same configuration. In their experiment, the ratio of the incoming boundary-layer thickness, defined at  $x/L = -0.65$ , to the bump height varies from about 0.083 to 0.1 as the Reynolds number decreases within the stated range.

A number of experimental investigations for similar configurations were undertaken in the past but usually came with certain caveats. For example, Baskaran et al. [4] did a thorough investigation concerning the interaction of a low-speed turbulent boundary layer, at a momentum-thickness Reynolds number of  $Re_\theta \approx 6000$ , with a two-dimensional curved hill, similar in shape to the current bump, and examined the

formation of an internal layer triggered by the surface curvature discontinuity. The ratio of the upstream boundary-layer thickness to the hill height was  $\delta/h = 0.4$ . Even though the flow separated in the adverse pressure gradient region, the measurements and the analysis in that work were mostly focused on the attached flow upstream of separation and the internal layer developing in it. Webster et al. [5] examined the passage of a low-speed turbulent boundary layer at  $Re_\theta \approx 4030$  over a two-dimensional bump and took fairly detailed measurements of the flowfield. The ratio of the upstream boundary-layer thickness to the bump height was  $\delta/h = 1.5$ . Internal layers were observed to form as a result of the surface curvature discontinuity at the leading and trailing edges of the geometry. The flow experienced significant changes in its mean state and turbulent stresses as it moved over the bump, but did not separate under the adverse pressure gradient. The lack of separation in this experiment limited its usefulness to computational efforts related to separation prediction. Another well-known experimental investigation is the NASA wall-mounted hump flow by Greenblatt et al. [6]. This experiment examined the separation of a low-speed turbulent boundary layer that started off at  $Re_\theta \approx 6500\text{--}7200$ , corresponding to an inflow  $\delta/h \approx 0.57$ , as it moved over a wall-mounted hump, representative of the upper surface of a subsonic airfoil. Although an extensive experimental dataset is available for this flow, the use of end plates in combination with a narrow-span model introduced certain three-dimensionality effects into the flow development that are prohibitively expensive to include in the simulations. Hence, meaningful comparisons between this experimental dataset and the simulations that commonly invoke the spanwise periodicity assumption are hard to make for this test case.

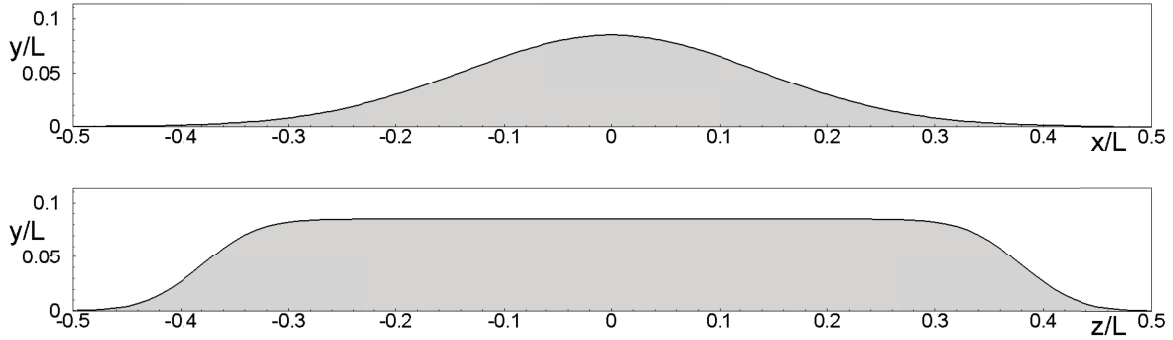


**Figure 1. Upper, side view; lower, spanwise cross-section; side walls are at  $z/L = \pm 0.5$ , ceiling is at  $y/L = 0.5$  (courtesy of Dr. Philippe Spalart).**

The speed bump experiment, depicted in Figure 1, can be considered a fresh attempt to overcome some of the shortcomings of the previous investigations and gather high-quality data using modern instrumentation that can be used in the validation of ongoing computational efforts related to smooth body flow separation. The tapered model ends used in this test case are intended to minimize the tunnel end-wall effects on the centerline region of the flow. The experimental measurements by Williams et al. [2] [3] suggest that the three-dimensionality effects on the centerline region are not particularly strong. To provide further evidence related to this point, the surface pressure distribution obtained from the present spanwise-periodic simulation will show reasonable agreement with the corresponding experimental measurement taken on the centerline at a similar Reynolds number [3].

Several groups have recently studied the speed bump flow problem using various turbulence modeling approaches, including direct numerical simulation (DNS). For example, spanwise-periodic DNS results have been recently reported by Uzun and Malik [7], [8], as well as by Balin et al. [9]. Both of these simulations were performed at a Reynolds number of  $Re_L = 1$  million (bump height Reynolds number of 85000), with a domain span of  $0.04L$ , where  $L$  is the width of the experimental model. The comparisons between the corresponding Reynolds-averaged Navier-Stokes (RANS) calculation predictions and the DNS results

were found unsatisfactory. Other results from lower-fidelity simulations, in the form of improved delayed detached eddy simulation (IDDES) by Balin et al. [9], and wall-modeled large-eddy simulation (WMLES) by Iyer and Malik [10], have also been reported and showed mixed success, once again underlining the need for improved wall and turbulence models to better predict these types of flows. Wright et al. [11] performed a hybrid LES-DNS at  $Re_L = 1$  million, in which the near-wall region of the flow was computed using DNS, and LES was employed in the outer region. This hybrid approach worked reasonably well in the attached flow upstream of separation, but showed some deficiencies in the adverse pressure gradient region where incipient separation is expected at this Reynolds number.

The current effort is a continuation of our recent work on the speed bump flow. The relatively low Reynolds number of  $Re_L = 1$  million used in our first DNS and the additional stabilizing effect of convex surface curvature were found to cause a tendency toward relaminarization or stabilization in the acceleration region. The flow experienced incipient or weak separation in the adverse pressure gradient region. Similar observations have been reported by Balin et al. [9] in their work. In practical applications, the Reynolds number is generally high enough to preclude relaminarization or stabilization under acceleration and/or convex surface curvature. Hence, in order to truly test and improve the turbulence models used in lower-fidelity simulation tools for high Reynolds number applications, reliable data from a test case that does not contain any relaminarization are needed. A test case that generates more severe separation under adverse pressure gradient conditions is also desirable for the evaluation of model performance in such flows. These needs provide the motivation for the present study, which repeats the simulation at the higher value of  $Re_L = 2$  million (bump height Reynolds number of 170000). Due to limited computational resources, full DNS resolution cannot be afforded everywhere; hence, the simulation is performed as a hybrid DNS and wall-resolved large-eddy simulation (WRLES) as described below. A DNS or a WRLES of the full experimental configuration, at a reasonably high Reynolds number, is highly desirable but would be well beyond the reach of the currently available computing capability. Although the present spanwise-periodic calculation cannot duplicate the experimental configuration, the data obtained from this simulation can still serve as a useful validation benchmark for the lower-fidelity simulation methods performed under similar conditions, before those tools are applied to more complex cases with better confidence.

The paper is organized as follows. Section 2 gives the details of the computational methodology used in this study. Analysis of the simulation results are provided in section 3. Section 4 summarizes the findings and provides the concluding remarks.

## 2 Computational methodology

Our first DNS for the problem at hand was performed at  $Re_L = 1$  million using a new compressible flow solver developed exclusively for GPUs [7], [8]. For the current simulation at  $Re_L = 2$  million, which requires 10.2 billion grid points for a span of  $0.08L$ , a sufficient number of GPUs was not available to make use of the GPU flow solver. Therefore, the present simulation is performed with a flow solver developed for central processing units (CPUs), which was used to study a number of problems in the past. This CPU code was most recently used for the simulation of the low-speed flow separation around the NASA wall-mounted hump [12], and for the Bachalo-Johnson transonic shock-induced flow separation problem using as many as 24 billion grid points [13].

The CPU code solves the unsteady three-dimensional compressible Navier-Stokes equations discretized on multiblock structured and overset grids. It employs an optimized prefactored fourth-order accurate compact finite-difference scheme [14] to compute all spatial derivatives in the governing equations. This optimized scheme offers improved dispersion characteristics compared to the standard sixth- and eighth-order compact schemes [15]. It is derived from the standard eighth-order compact scheme that has been shown to possess “spectral-like” resolution [15]. Third-order one-sided and biased schemes, respectively, are used on

a boundary point and on the point next to the boundary. To eliminate the spurious high-frequency numerical oscillations that may arise from several sources (such as grid stretching, unresolved length scales and approximation of physical boundary conditions) and ensure numerical stability, we also employ high-order (up to tenth-order) compact filtering schemes [16], [17]. The present simulation uses the tenth-order filtering scheme, with matching one-sided biased formulations near the physical boundaries [16]. Instead of using an explicit subgrid-scale (SGS) model, the numerical dissipation of the spatial filtering operation is chosen to serve as an implicit SGS model for LES. A Beam-Warming type approximately factorized implicit scheme with subiterations is used for the time advancement [18]. More details of the simulation methodology can be found in publications by Uzun and coworkers [19], [20], [21], [22].

### 3 Spanwise-periodic flow simulation over the speed bump at $Re_L = 2$ million

The equation describing the full three-dimensional speed bump geometry [1] is given by

$$y(x, z) = \frac{h}{2} \left[ 1 + \operatorname{erf} \left( \left( \frac{L}{2} - 2z_0 - |z| \right) / z_0 \right) \right] \exp \left( -(x/x_0)^2 \right) \quad (1)$$

where  $x, y, z$  respectively, denote the axial, vertical and spanwise directions,  $L$  is the width of the experimental model that is taken as the reference length scale,  $h = 0.085L$  (bump height),  $x_0 = 0.195L$  and  $z_0 = 0.06L$ . For the present spanwise-periodic simulation that assumes a uniform profile along the span, the two-dimensional profile shape is given by  $y(x) = h \exp \left( -(x/x_0)^2 \right)$ .

#### 3.1 Simulation details

The Reynolds number based on the upstream reference velocity,  $U_\infty$ , and  $L$  is  $Re_L = 2$  million, while the freestream Mach number is selected as 0.2. The corresponding Reynolds number based on  $h$  is 170000. The periodic domain span is set to  $0.08L$ . A schematic of the computational domain is provided in Figure 2. The inflow boundary of the domain is at  $x/L = -0.8$  while the outflow boundary is at  $x/L = 2$ . The physical domain ends at  $x/L = 1$ . The region from  $x/L = 1$  to 2 forms the sponge zone, in which rapid grid stretching is applied along the streamwise direction. This zone contains only a few hundred points because of the significant grid stretching applied. The sponge zone dampens the turbulence in the flowfield before it reaches the outflow boundary, where standard characteristic outflow boundary conditions are applied. Viscous isothermal boundary conditions are imposed on the lower boundary, which contains the speed bump profile. The uniform wall temperature is set the same as the reference freestream value. The outer boundary in the vertical direction is placed at  $y/L = 1$ , on which a nonreflecting characteristic boundary condition is applied. This choice of a nonreflecting characteristic boundary condition on the outer boundary was made based on the observation that a spanwise-periodic simulation cannot accurately model the effects associated with the tapered ends of the experimental model and the tunnel side walls. Therefore, because we are already not faithfully modeling the entire wind tunnel conditions, the decision was made to simplify the treatment of the upper boundary.

The domain is discretized using 15360 points along the streamwise direction, 384 points in the vertical direction and 1728 uniform points along the spanwise direction. The total number of grid points is about 10.2 billion. Figure 3 plots the variation of streamwise, wall-normal and spanwise grid resolutions in terms of wall units, respectively, denoted as  $\Delta s^+$ ,  $\Delta n^+$  and  $\Delta z^+$ , along the wall. Upstream of the bump, we see that  $\Delta s^+ < 9$ , while  $3 < \Delta z^+ < 4$ . Once the flow enters the acceleration region,  $\Delta s^+$  decreases a bit more and then settles to a value of around 8, while  $\Delta z^+$  starts to increase and reaches a maximum value of around 6 near the apex. As we have a uniform spacing along the span, the maximum  $\Delta z^+$  position coincides with the peak wall skin-friction location, which is found near the apex. These spacings quickly decrease as the flow starts decelerating past the apex and moves toward separation. In the separated region, the largest values of

$\Delta s^+$  and  $\Delta z^+$  are less than 7 and 2, respectively. Once the flow recovers from the separation, these spacings start to increase once more. Toward the end of the physical domain, the largest  $\Delta s^+$  and  $\Delta z^+$  become about 12 and 3.5, respectively.

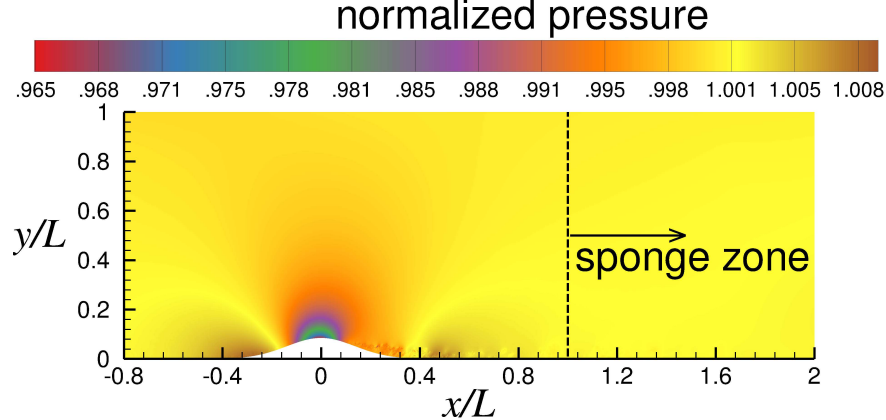


**Figure 2. Computational domain schematic. Contours denote the instantaneous pressure normalized by the reference value.**

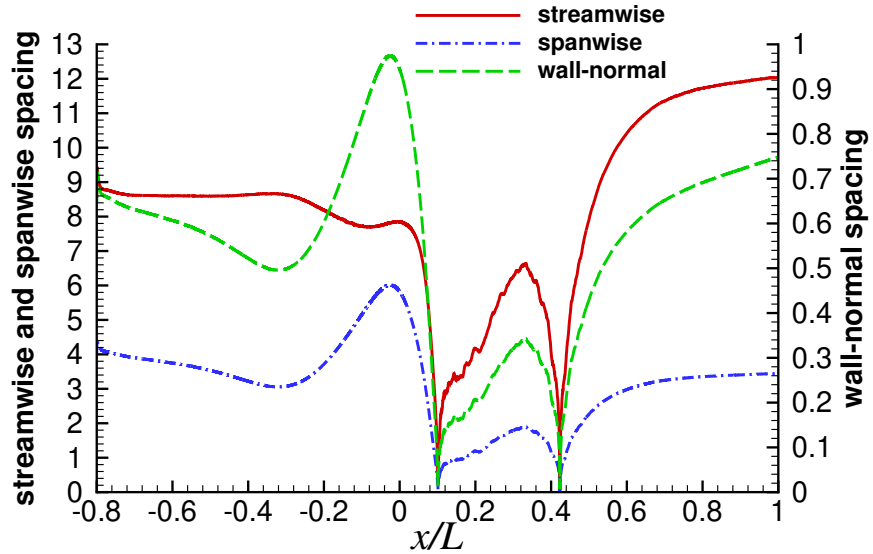


**Figure 3. Near-wall grid spacings in wall units.**

The wall-normal grid spacing,  $\Delta n^+$ , on the wall generally varies from 0.5 to 1 in the attached region and becomes smaller in the separated region. The wall-normal spacing increases with distance from the wall. In the region upstream of the bump, the largest  $\Delta n^+$  found in the vicinity of the attached boundary-layer edge is around 5–7 units. In the acceleration region, the maximum corresponding value is about 14 units. In the downstream recovery region, the largest  $\Delta n^+$  values around the boundary-layer edge are found near the end of the physical domain, and have a value of about 50. These outer region spacings get relatively larger in the recovery region because the reattached boundary layer is considerably thicker than that prior to separation, and at the same time, there is a limit on the number of grid points that can be afforded in the

wall-normal direction. The thickest section of the separation bubble is about  $0.057L$  in height (as measured from the lower wall), and is discretized using about 305 out of the total 384 points in the vertical direction. The largest vertical grid spacing at the outer edge of separated region is around  $10^{-3}L$ . The separated region is covered by nearly 2000 points along the streamwise direction.

The  $\Delta s^+$  and  $\Delta z^+$  values in much of the domain are comparable to those used in turbulent boundary-layer simulations performed using spectral methods. Those methods normally use a  $\Delta s^+$  of about 10 units, and a  $\Delta z^+$  of 4–5 units. Their  $\Delta n^+$  on the wall is typically less than 1, and the largest  $\Delta n^+$  at the boundary-layer edge is on the order of the  $\Delta s^+$ . We see that the near-wall grid resolutions used in the present simulation, performed with a fourth-order accurate compact finite-difference scheme, are not too far off from those used in spectral methods to perform a DNS. The present simulation approaches DNS or “quasi-DNS” resolution in almost the entire region prior to separation. However, our outer region resolution in the wall-normal direction within the downstream recovery zone is several times coarser than what would be needed in a DNS. Based on these observations, the present simulation can be best categorized as a hybrid DNS-WRLES (without any explicit SGS model).

The second-order accurate implicit Beam-Warming scheme [18] is used for the time integration. The time step taken in the simulation corresponds to a maximum Courant-Friedrichs-Lowy (CFL) number of 5. It takes 178,955 time steps to compute a time interval of  $L/U_\infty$ . The solution is filtered at every time step using the tenth-order compact filter with a filtering parameter of  $\alpha_f = 0.49$  [16], [17], which is known to provide a minimal amount of numerical dissipation from an earlier study [23]. For the simulation, nearly 40000 Intel Skylake cores, located at the NASA Advanced Supercomputing Division at the Ames Research Center, are used. The simulation takes about 40 days of run time to compute a time interval of  $13L/U_\infty$ . To minimize the duration of the initial transient period, the simulation is started from the previous solution available at  $Re_L = 1$  million as the initial condition. The initial numerical transients are driven out of the computational domain during the first  $2L/U_\infty$ . Statistical data are gathered over the remaining  $11L/U_\infty$ , which covers 6.1 physical domain flow-through times.

For the turbulent inflow generation, we employ a version of the rescaling-recycling technique discussed in Uzun and Malik [13], [8]. The present technique only recycles the turbulent fluctuations while keeping the mean inflow profile fixed. The mean flow imposed at the inflow boundary is taken from a RANS calculation performed with the low-Reynolds-number correction version of the Spalart-Allmaras model [24]. The mean inflow boundary-layer thickness at  $x/L = -0.8$  is  $\delta_{in} \approx 0.0055L$ , giving  $\delta/h \approx 0.065^*$ . The corresponding inflow momentum-thickness Reynolds number is  $Re_\theta \approx 1035$ . The distance between the inflow and recycle planes is about  $12\delta_{in}$ . To check the performance of the inflow generation method, Figure 4 shows the comparison of mean streamwise velocity and Reynolds stress component profiles in wall units at  $x/L \approx -0.709$ , where  $Re_\theta = 1410$ , with the zero pressure gradient turbulent boundary-layer DNS data of Schlatter and Örlü [25] at the same  $Re_\theta$ . This station is located about  $16.5\delta_{in}$  from the inflow plane. In the figure,  $u'u'$ ,  $v'v'$ ,  $w'w'$  and  $u'v'$  represent the streamwise, wall-normal, spanwise and shear components of the Reynolds stress, respectively. We find very good overall agreement in all profiles. The differences could be due to the different numerics, and the potential effects of the weak adverse pressure gradient upstream of the bump, as well as the particular mean inflow conditions taken from the RANS calculation in the present case.

### 3.2 Simulation results

We now discuss the main findings. Whenever appropriate, in order to discuss Reynolds number related effects, reference will be made to our previous results for  $Re_L = 1$  million, obtained using a different fourth-order accurate solver developed for GPUs [7] [8]. To reiterate, the incoming boundary-layer  $Re_\theta$  value

---

\*Based on the boundary-layer thickness at  $x/L = -0.65$ , where the experimental inflow  $\delta$  is defined, the equivalent value is  $\delta/h = 0.1$ .

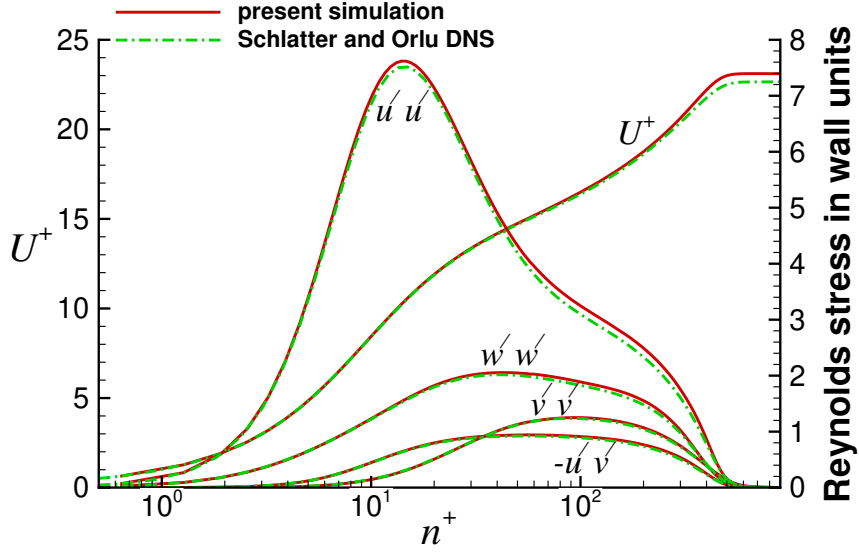


**Figure 4.** Mean streamwise velocity and Reynolds stress component profile comparisons at  $Re_\theta = 1410$ .

is 1035 for the  $Re_L = 2$  million case, and 530 in the  $Re_L = 1$  million case. As noted earlier, one of the motivations for performing a simulation at the present higher  $Re_L$  value is to have a case that assures significant flow separation in the adverse pressure gradient region, which would be useful for the evaluation of lower-fidelity simulation tools. Figure 5 depicts a snapshot of the normalized total vorticity magnitude contours in an  $x - y$  plane for the present simulation at  $Re_L = 2$  million and the previous DNS at  $Re_L = 1$  million. The flow visualizations show that the flow past the apex in the  $Re_L = 1$  million case experiences very weak separation relative to that observed in the higher  $Re_L$  case. As discussed in Uzun and Malik [7], [8], the time-averaged statistics for the lower  $Re_L$  case verify the incipient or very weak separation in the range where  $0.195 \lesssim x/L \lesssim 0.268$ . The separated flow in the  $Re_L = 2$  million case is evident in the form of the shear layer represented by high levels of vorticity, and the reversed flow region beneath this shear layer, which contains relatively lower vorticity levels. The subsequent reattachment of this separated flow further downstream generates a thicker boundary layer compared to that found in the same region of the lower  $Re_L$  case. Hence, we observe that the chosen  $Re_L = 2$  million case is indeed successful in generating stronger flow separation in the adverse pressure gradient region. The reason for the resistance of the lower  $Re_L$  flow against separation is explored in the upcoming analysis. Another important difference between the two cases is the tendency toward relaminarization or stabilization very near the wall upstream of the apex in the lower  $Re_L$  case, which is not clearly visible in the shown vorticity snapshots. The absence of relaminarization/stabilization in the higher  $Re_L$  case will also be verified in the upcoming analysis.

### 3.2.1 Overview of the main flowfield features

We first examine the variation of several quantities that are representative of the main features of the flow at  $Re_L = 2$  million as it moves over the bump. The first quantity of interest is the mean boundary-layer thickness,  $\delta$ , scaled by  $L$ . This is determined using a procedure based on the mean spanwise vorticity, as discussed in Uzun and Malik [7], [8]. The second quantity is the boundary-layer edge velocity,  $U_e$ , which is computed from an integral of the mean spanwise vorticity [26], [7], [8], and scaled by  $U_\infty$ . Surface pressure

and skin-friction coefficients are the other quantities of interest. These coefficients are given by

$$C_p = \frac{p - p_\infty}{\frac{1}{2}\rho_\infty U_\infty^2} \quad \text{and} \quad C_f = \frac{\tau_w}{\frac{1}{2}\rho_\infty U_\infty^2} \quad (2)$$

where  $\rho_\infty$ ,  $p_\infty$ ,  $U_\infty$ , respectively, are the reference freestream density, pressure and velocity,  $p$  is the mean surface pressure and  $\tau_w$  is the mean wall shear stress. The  $C_p$  distribution is compared with the data taken on the centerline of the experiment by Williams et al. [3]. Experimental  $C_f$  data were not available. The  $C_f$  distribution is compared with the data from a compressible RANS calculation performed with the low-Reynolds-number correction version of the S-A model (low-Re S-A model) [24] under conditions identical to those in the present simulation.

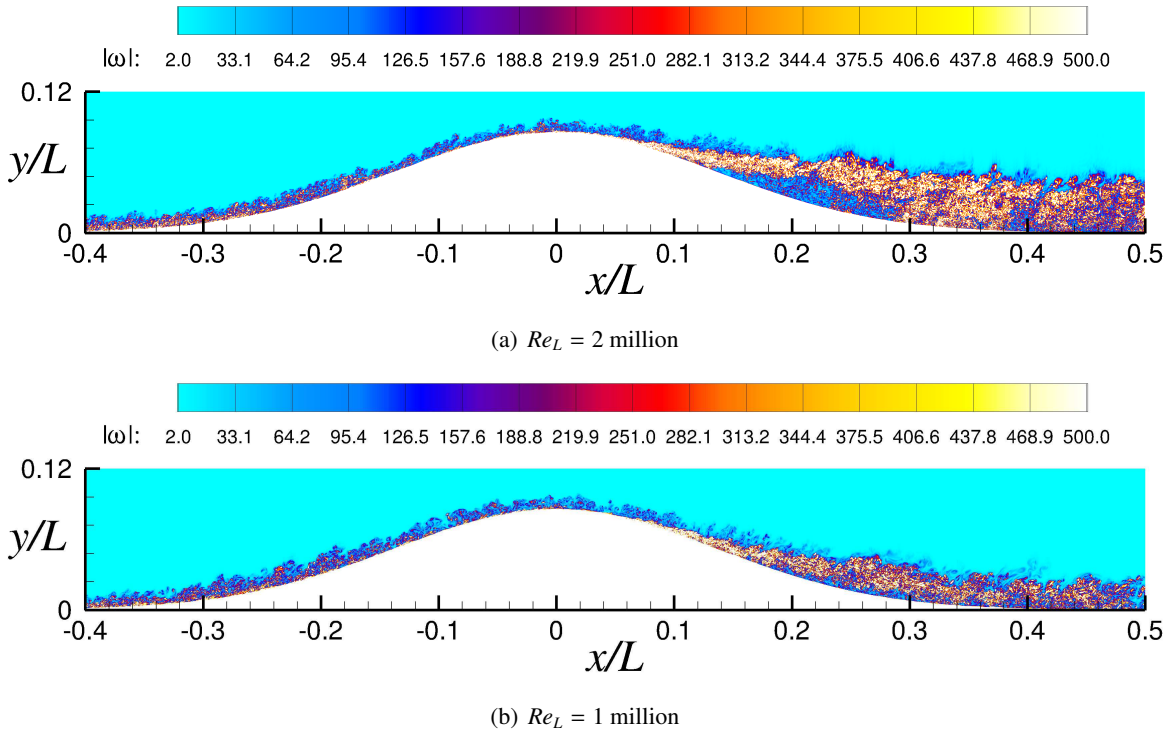


**Figure 5. Instantaneous normalized total vorticity magnitude contours on an  $x - y$  plane.**

Figure 6 plots the variation of  $\delta/L$ ,  $U_e/U_\infty$ ,  $C_p$  and  $C_f$ . All quantities experience significant changes as the flow moves over the bump. The incoming boundary layer encounters an initially mild adverse pressure gradient and thus shows a linear growth in  $\delta/L$  far upstream of the bump. The adverse pressure gradient becomes progressively stronger as the flow approaches the bump foot, and causes the associated decreases in  $U_e$  and  $C_f$  in the upstream region. The pressure gradient becomes strongly favorable starting at  $x/L \approx -0.29$  until very near the bump apex. The accelerated flow sees a significant increase in  $U_e$ , which takes a maximum value of about  $1.5U_\infty$  slightly upstream of the apex. The flow acceleration also increases the  $C_f$  because of the steepening near-wall velocity gradient, while simultaneously reducing the boundary-layer thickness, as shown by the corresponding drop in  $\delta/L$ . The  $C_f$  peak is reached at  $x/L \approx -0.024$ .

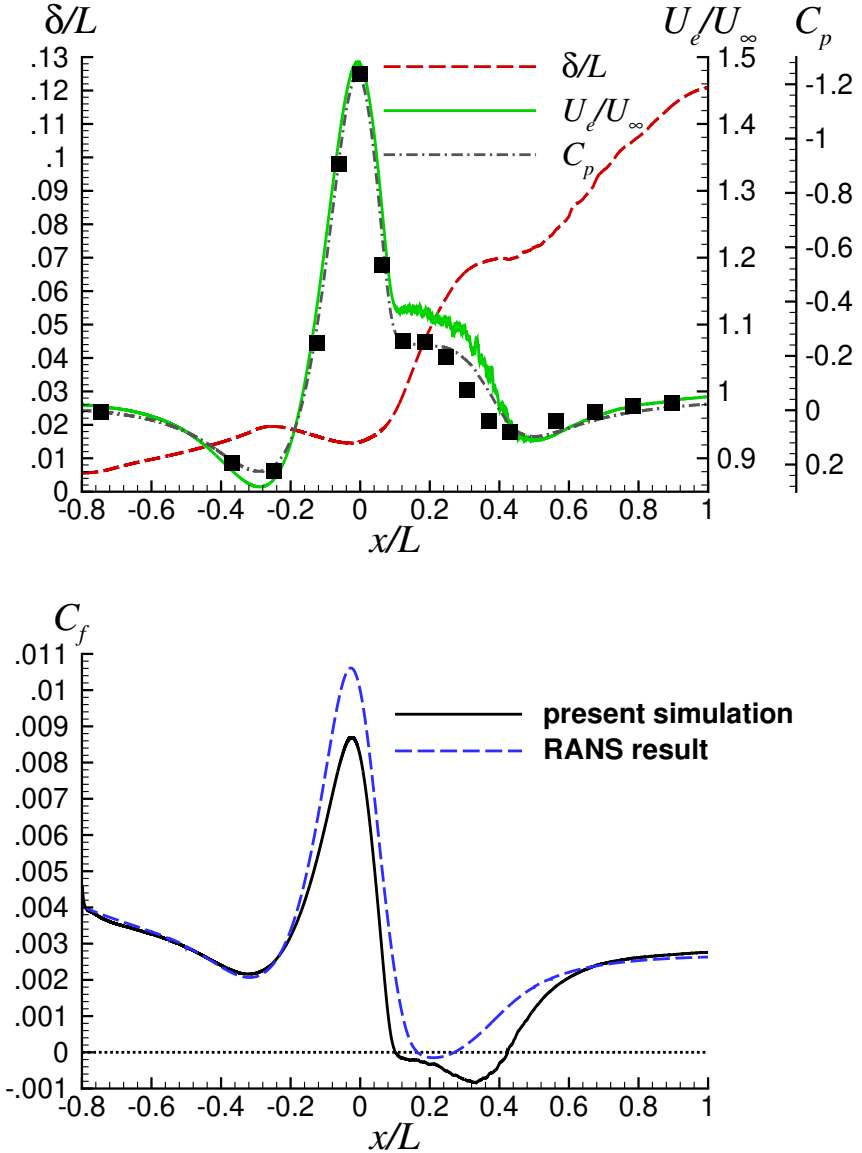


**Figure 6.** Streamwise variation of  $\delta/L$ ,  $U_e/U_\infty$ ,  $C_p$  and  $C_f$ . Symbols denote the experimental  $C_p$  measurement.

The pressure gradient becomes adverse immediately after the apex, and slows down the flow. The deceleration leads to strong separation at about  $x/L = 0.1$ , as discussed earlier during the examination of Figure 5. The flow separation is also verified by the negative  $C_f$  distribution, which indicates a fairly broad reversed flow region. The reattachment is at  $x/L = 0.42$ . The plateau encountered in the  $C_p$  distribution as the pressure increases from the apex to the tail of the bump is a footprint of the separated flow. The pressure gradient becomes mildly favorable around the tail of the bump, as the flow recovers from the separation. Note that  $U_e/U_\infty$  consistently follows the pressure gradient in the aft region as it does elsewhere. It decreases as pressure increases and vice versa. The boundary-layer thickness rapidly rises in the deceleration region and briefly plateaus around the tail of the bump, where the pressure gradient becomes favorable again, before continuing to increase. The separated flow naturally generates large structures, whose reattachment leads

to the formation and further evolution of a thick boundary layer in the recovery zone, as depicted earlier in Figure 5. We should note here that the methods employed to determine the boundary-layer thickness and the corresponding edge velocity in this study do not distinguish between attached and separated flows. The notion of a boundary-layer thickness or an edge velocity in the separated region is ambiguous, at best; nevertheless, these methods provide a seamless transition in these boundary-layer quantities as the attached flow separates and then reattaches.

The boundary-layer thicknesses found in the deceleration region of the flow past the apex and further downstream become comparable to and eventually exceed the span of  $0.08L$  used in the simulation. Thus, the flow development in those regions would be affected to some extent by the constraint imposed by a narrow span. However, we do not expect this constraint to completely overwhelm the dynamics at play. The flow would still separate in a simulation performed with a wider span, but the growth rate of the shear layer would likely be different in such a case. Thus, the wider span would be expected to affect the reattachment point of the separated flow. Similarly, the statistical properties of the reattached flow recovering from separation would likely be influenced by the span. Given the limited access to computational resources, repeating the simulation on a wider domain span was not possible at the time of this writing.

Examining the  $C_p$  distribution further, we observe reasonable overall agreement between the present simulation and the experimental data from Williams et al. [3]. This experiment was performed for a Reynolds number of about 2 million but at a freestream Mach number of 0.1. The good agreement observed in the peak  $C_p$  between the present simulation and the experiment suggests that any blockage effect of the ceiling in the experiment is largely countered by the tapered end effects of the 3-D bump geometry. Recall that neither of those effects were accounted for in the current simulation. The pressure or  $C_p$  plateau found in the separated region, identified in our earlier analysis, is also verified by the experimental observation. The pressure rise observed after the plateau appears slightly delayed in the simulation relative to the experiment, which suggests that the reattachment location in the simulation will likely be slightly delayed relative to the experiment. This difference perhaps should not be a surprise given the upstream Mach number mismatch and the fact that no attempt was made to model all effects present in the experiment. These observations also suggest that the end effects on the centerline region of the experimental flow are not particularly strong. Hence, the separation phenomenon encountered around the centerline of the experimental geometry is not too fundamentally different from that generated in a spanwise-periodic simulation despite the counterrotating vortices observed in the experiment.

Comparison of the computed  $C_f$  distribution with the corresponding RANS result shows that the RANS prediction is unsatisfactory. In contrast to the present simulation, the RANS  $C_f$  result indicates very weak or incipient separation. Upstream of the bump, there is reasonable agreement in the  $C_f$  predictions. However, differences start to appear as the flow starts accelerating, and the peak  $C_f$  in the RANS result is found to be considerably higher. Such shortcomings of the RANS calculations are not surprising and provide one of the motivations for the present study.

### 3.2.2 Examination of the region upstream of the apex

We now examine the region upstream of the apex. We first verify that the present flow at  $Re_L = 2$  million does not experience the relaminarization/stabilization encountered at half the Reynolds number [7], [8] and discuss the curvature related effects. We then analyze the mean streamwise velocity and Reynolds stress profile evolutions.

**Verification of the absence of relaminarization/stabilization:** One of the goals of this study is to simulate a high enough Reynolds number flow that does not relaminarize or stabilize in the acceleration region prior to separation. To check whether this goal has been achieved with the present  $Re_L$  case, Figure 7 plots the variation of two parameters that could be helpful in detecting relaminarization or reverse transition. The

first parameter is the acceleration parameter,  $\Delta_p$ , and the second one is the relaminarization parameter,  $K$ . These parameters are defined as

$$\Delta_p = -\frac{\nu}{\rho u_\tau^3} \frac{\partial p}{\partial s} \quad \text{and} \quad K = \frac{\nu}{U_e^2} \frac{\partial U_e}{\partial s} \quad (3)$$

where  $\nu$  is the kinematic viscosity,  $\rho$  is the density,  $u_\tau$  is the wall friction velocity,  $p$  is the surface pressure,  $U_e$  is the boundary-layer edge velocity, and  $s$  is the surface distance along the wall.

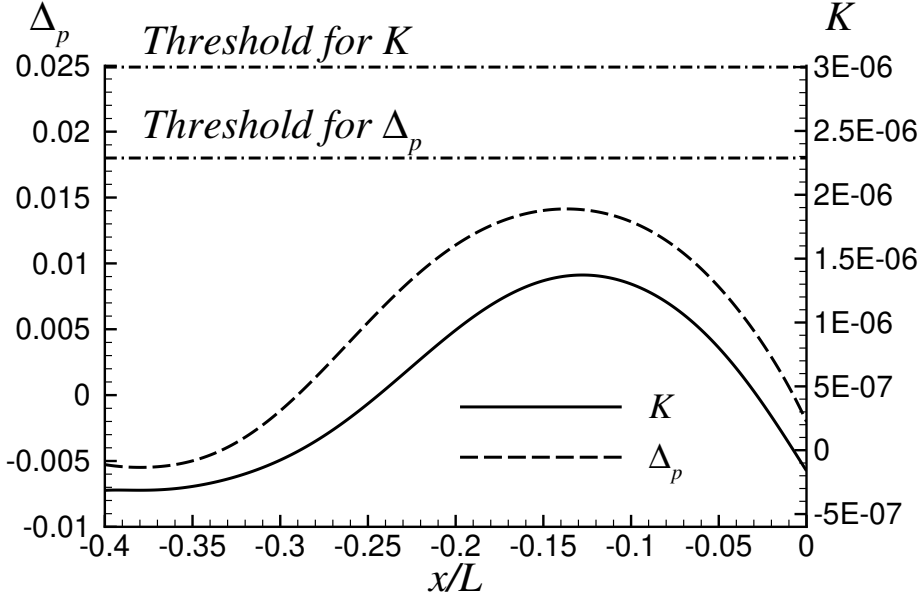


**Figure 7. Variation of acceleration and relaminarization parameters.**

We observe that the peak  $K$  value stays well below the commonly accepted threshold value of about  $3 \times 10^{-6}$  [27], [28], [29]. Similarly, the  $\Delta_p$  parameter never reaches the threshold value of 0.018 determined by Patel and Head [30], who concluded that “major departures” from the logarithmic layer occur when this parameter exceeds this value. They believe this major departure to be an indication of the onset of relaminarization or reverse transition. The analysis presented in Refs. [7], [8] confirmed that this particular threshold of  $\Delta_p$  is a reasonable predictor of the logarithmic layer disappearance in the acceleration region of the previous simulation performed at  $Re_L = 1$  million, even though the  $K$  parameter never reached its corresponding threshold value in that case. There is also the stabilizing effect of convex surface curvature, which becomes stronger as the flow approaches the apex. Consequently, in the  $Re_L = 1$  million case, the accelerating flow experiences relaminarization/stabilization over the upstream half of the speed bump, as discussed in Refs. [7], [8]. For the present higher  $Re_L$  case, the fact that  $\Delta_p$  never reaches the threshold value suggests that the turbulence is able to survive the strong acceleration and convex curvature effects without relaminarization/stabilization.

To provide further verification for the lack of relaminarization/stabilization in the present simulation, Figure 8 depicts the total velocity magnitude contours near the wall, normalized by the reference freestream velocity, in the region where  $-0.5 < x/L < 0.1$ . On this plane, the wall-normal distance in wall units varies from about 3 to 6, except near  $x/L = 0.1$  where the flow is about to separate. The region of interest is shown as two separate subfigures and the maximum value of the contour range differs between the two subfigures. At this particular  $Re_L$ , the near-wall streaks are rather narrow; hence, for clarity, a ratio of two to one between the vertical and horizontal axes has been used in these visualizations. The near-wall

streaks shown in the top subfigure verify a fully turbulent upstream boundary layer approaching the bump. The bottom subfigure shows no evidence of relaminarization/stabilization as the accelerated boundary layer moves toward the apex. Similar near-wall flow visualizations of the lower  $Re_L$  flow, which can be found in Refs. [7], [8], showed clear evidence of relaminarization/stabilization in that case. We also observe localized spots containing relatively high instantaneous total velocity magnitudes as the accelerated flow approaches the apex in the present case. This is because the fuller velocity profile of the turbulent boundary layer in the higher  $Re_L$  case is able to sustain localized patches of higher instantaneous velocities close to the wall in that region. The flow separates shortly after it enters the adverse pressure gradient region, at  $x/L \approx 0.1$ , as evidenced by the very low or nearly zero velocities at that station. As seen in Figure 5, the lower  $Re_L$  flow is still fully attached at that location. The reason for the resistance of the lower  $Re_L$  flow against separation is explored later.

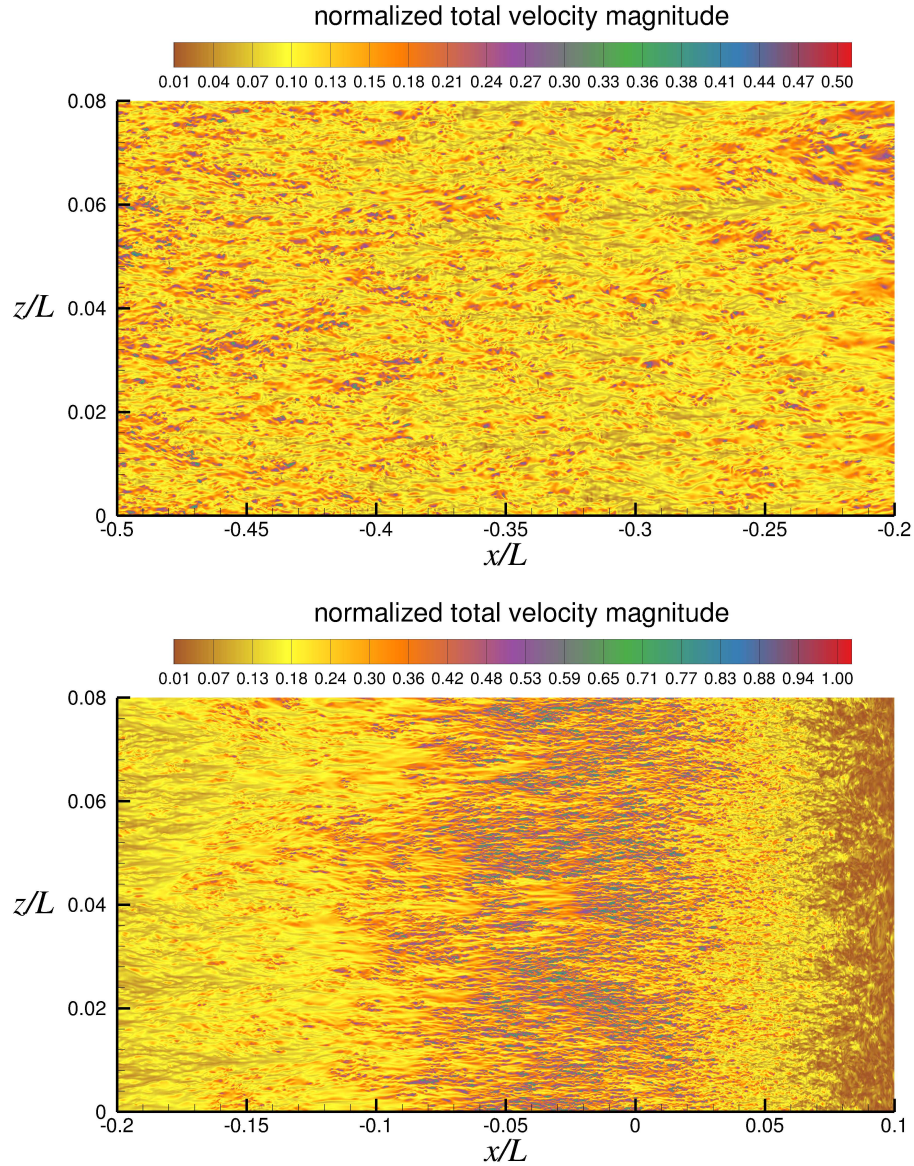


**Figure 8. Normalized total velocity magnitude contours near the wall.**

**Surface curvature related effects:** Previous work on surface curvature effects on turbulent boundary layers showed that convex curvature has a stabilizing effect on turbulence and leads to a reduction in Reynolds stresses and skin friction [31], [32], while concave curvature has a destabilizing effect that increases Reynolds stresses and skin friction [33], [34]. These observations originate from the studies that maintain negligible or minimal pressure gradient along the flow direction while the surface curvature is introduced to the incoming turbulent boundary layer. The present bump geometry has convex curvature in the range where  $-0.138 \lesssim x/L \lesssim 0.138$  and concave curvature elsewhere. Curvature effects in the present problem are obscured by the favorable and adverse pressure gradients in the corresponding sections of the bump. For example, in the late stages of flow acceleration toward the apex, the surface curvature becomes convex once the flow goes past  $x/L \approx -0.138$ , but  $C_f$  still increases until very near the apex despite the convex curvature, which is supposed to decrease  $C_f$  under zero pressure gradient. This suggests that the strong favorable pressure gradient is able to steepen the near-wall velocity gradient magnitude and work against the opposite effect of convex curvature on  $C_f$ . As noted earlier, the  $C_f$  distribution peaks at  $x/L \approx -0.024$ , and then starts its descent. The favorable pressure gradient begins to ease as the apex is approached. The decrease in the  $C_f$  beginning slightly upstream of the apex is likely the combined outcome of the convex curvature eventually kicking into effect<sup>†</sup> as the favorable pressure gradient vanishes, and the nascent adverse pressure gradient effect.

In their review of work related to turbulent boundary layers on concave surfaces, Barlow and Johnston [35] noted that some of the previous investigators reported large spanwise variations in the statistical properties of the flow, which were attributed to the formation of longitudinal vortices, also referred to as roll cells, while others found no such significant variations. These types of structures are believed to be generated by the same centrifugal instability mechanism that produces the well-known Taylor-Görtler vortices in a laminar boundary layer over a concave surface [36]. Evidence suggests that the spanwise nonuniformities in the upstream mean flow can have an important effect on the location of roll cells observed over concave surfaces. Such disturbances on the mean flow can be generated by the turbulence-damping screens in laboratory experiments, or they can also originate from more deliberate sources, such as an array of small vortex generators. It is therefore postulated that in cases where no evidence of stationary roll cells were observed, the upstream mean flow must have been largely free of nonuniformities. The observations made in their own investigation led Barlow and Johnston [35] to firmly conclude that distinct longitudinal vortices do not exist in a turbulent boundary layer over a concave surface when the upstream mean flow is free of spanwise nonuniformities. In such a case, they instead observed unsteady, randomly-distributed “large-eddy structures” with a streamwise extent of only a few boundary-layer thicknesses that did not cause any significant spanwise variations in the mean properties of the boundary layer. They also saw an increase in the skin friction over the concave surface, attributed to the enhanced mixing by these large-eddy structures that brings high-momentum fluid closer to the wall. In that experiment, the ratio of the incoming boundary-layer thickness to the concave radius of curvature,  $\delta/R$ , was about 0.07.

Based on these findings, the current understanding is that the upstream disturbances in the mean flow could be amplified by the concave curvature if such disturbances possess a certain spanwise wavelength that is within the range of the unstable wavelengths. The unstable range of wavelengths is known to be rather narrow and centered around a wavelength of about twice the boundary-layer thickness [34]. The coherent structures generated in turbulent boundary layers over concave surfaces can appear in the form of large steady vortices when the upstream disturbances are organized and of the proper unstable wavelength, and they could also be in the form of shorter nonstationary, randomly-distributed large eddies when the upstream boundary layer is uniform in the mean [35].

To see whether any major spanwise variations occur in the corresponding concave portion of the speed

---

<sup>†</sup>As will be seen shortly, the ratio of the local boundary-layer thickness to the radius of curvature surpasses 0.06 near the apex, which is believed to be high enough for the strong convex curvature effect to be felt under zero or weak pressure gradient conditions.

bump flow upstream of the apex, we examine the spanwise distribution of the time-averaged skin-friction coefficient at several streamwise stations in that region. The formation of any large stationary coherent structures over the concave surface would manifest itself as significant spanwise variations in the time-averaged skin-friction distributions. Figure 9 depicts the spanwise variation of the time-averaged skin-friction coefficient at several streamwise stations and the standard deviation from the mean spanwise-averaged value. The standard deviation is defined as

$$\sigma(C_f^z) = \sqrt{\frac{\sum (C_f^z - \bar{C}_f)^2}{N}} \quad (4)$$

where  $C_f^z$  is the time-averaged skin-friction coefficient at a given spanwise location,  $\bar{C}_f$  is the corresponding spanwise-averaged value and  $N$  is the number of spanwise grid points. The standard deviation is given in terms of the percentage of the mean spanwise-averaged value. To aid in the discussion, the bottom subfigure also includes the  $C_p$  and  $C_f$  distributions, as well as the ratio of the local boundary-layer thickness to the radius of curvature,  $\delta/R$ . The curvature changes from concave to convex at  $x/L \approx -0.138$ , where  $R$  goes to infinity, giving  $\delta/R = 0$  at that location.

We see in Figure 9 that all  $C_f^z$  distributions are fairly uniform along the span, and the maximum standard deviation is only about 2 percent of the corresponding mean value. According to the  $\delta/R$  variation shown in the bottom subfigure, the concave curvature effect would not be felt until the flow approaches  $x/L \approx -0.4$ . It is interesting to note that the standard deviation peaks at  $x/L \approx -0.29$ , around which the pressure gradient changes from mild adverse to strong favorable. This location also happens to be fairly close to where the peak  $\delta/R$  value of 0.036 is found over the concave surface, at  $x/L \approx -0.25$ . The standard deviation then decreases once the flow enters the strong-acceleration region and appears to level off in the region between the start of convex curvature at  $x/L \approx -0.138$  and the apex.

Hoffmann et al. [34] observed the generation of longitudinal vortices that induce significant changes to the turbulence structure with values of  $\delta/R = 0.01\text{--}0.02$  when small vortex generators were used to introduce organized disturbances upstream of the concave curvature in their experiment. The  $\delta/R$  values achieved in the concave region of the present flow are comparable to and greater than the values considered by Hoffmann et al. [34]. There is a mild adverse pressure gradient region that overlaps with the concave curvature, which is responsible for the skin friction decrease until  $x/L \approx -0.32$ . Note that  $\delta/R$  exceeds 0.01 beginning at  $x/L \approx -0.38$ , while the adverse pressure gradient ends at  $x/L \approx -0.29$ , downstream of which the strong favorable pressure gradient takes over. The boundary-layer thickness,  $\delta/L$ , grows with streamwise distance in this region, and its value at  $x/L = -0.38$  and  $-0.32$  is about 0.0154 and 0.0176, respectively. The distance from  $x/L = -0.38$  to  $-0.32$  is covered by less than 4 times the average boundary-layer thickness between those two stations. Concave curvature is normally expected to increase the skin friction under weak or negligible pressure gradient conditions. Because of the relatively short overlap region between the mild adverse pressure gradient and the concave curvature over which  $\delta/R$  values are reasonably large, the concave curvature appears to be mostly ineffective in increasing the skin friction against the opposite effect of the adverse pressure gradient. As noted above, the rise in the skin friction starts at  $x/L \approx -0.32$ , which is positioned toward the very end of the mild adverse pressure gradient. It is not clear whether the concave curvature plays any role in determining the exact location where this rise begins, as we would also expect an upstream influence of the nearby strong pressure gradient.

The relatively small variations observed in the spanwise skin-friction distributions suggest an absence of organized, stationary, vortical structures in the present flow. In order to understand why these variations are rather weak, we need to consider how the upstream fluctuations are generated in the present flow. Our inflow generation technique assumes a homogeneous fixed mean inflow profile along the span. The turbulent fluctuations imposed on the inflow plane are generated using the recycling/rescaling with dynamic reflection (RR+DR) technique introduced by Morgan et al. [37]. In this procedure, a reflection about a randomly chosen spanwise plane, or spanwise scrambling, is applied to the scaled fluctuations extracted from the

recycle plane before introducing them at the inflow plane. The spanwise reflection plane is updated at certain randomized intervals. These practices are intended to break down the coherence between the inflow and recycle planes, and also prevent the formation of any artificial energetic low-frequency structures in the flow. The turbulent fluctuations introduced at the inflow are made up of a spectrum of spanwise wavelengths. These fluctuations can be thought of as a range of disturbances simultaneously applied onto the mean flow, some of which may be amenable to further amplification by the interaction with the concave curvature. However, the disturbances generated on the mean flow in such a manner cannot be considered organized or stationary in the same sense the disturbances generated by the array of small vortex generators in the experiment of Hoffmann et al. [34] would be.

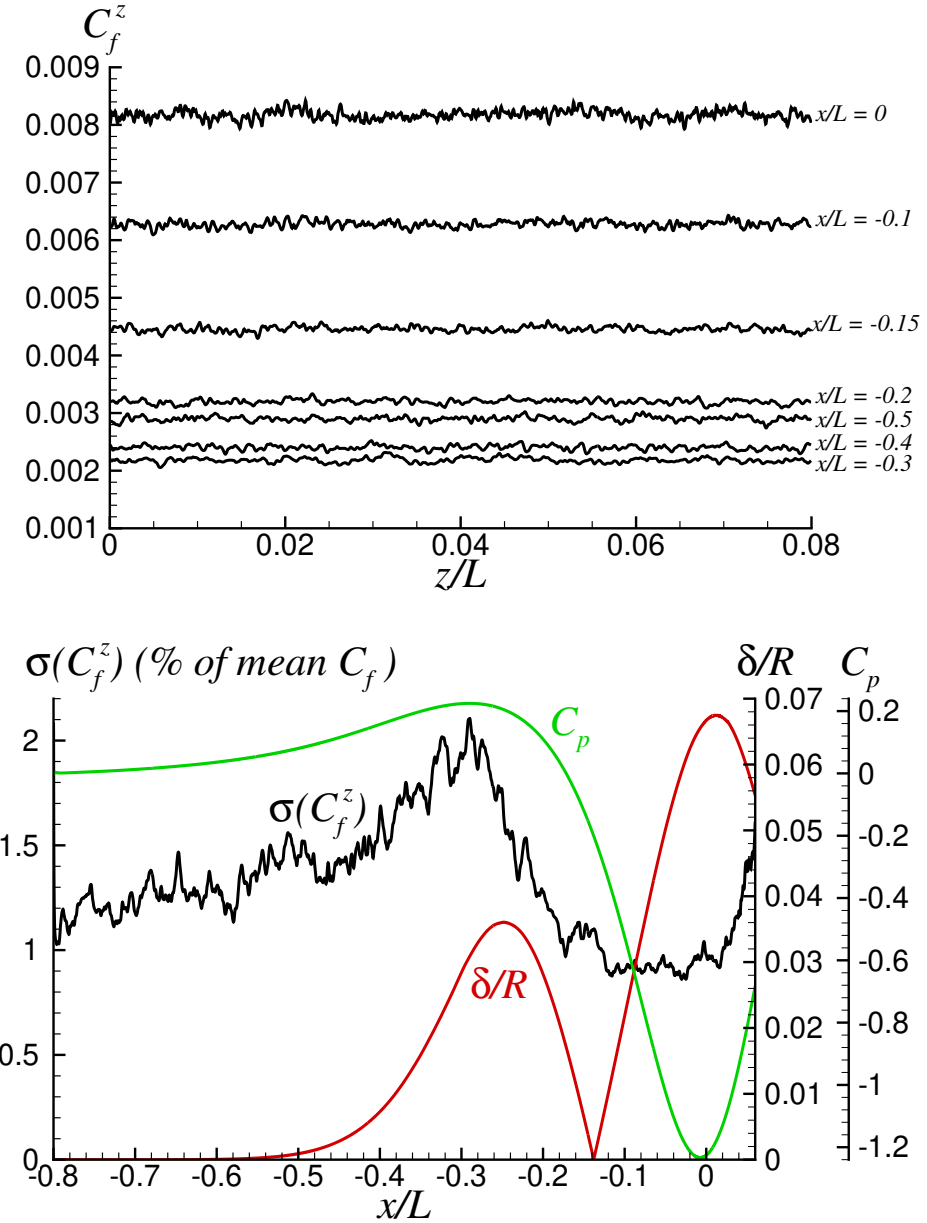


**Figure 9.**  $C_f^z$  distributions along the span and the streamwise variation of  $\sigma(C_f^z)$ .

Thus, it is plausible that the interaction between the concave curvature and the incoming disturbances with unstable wavelengths could generate some randomly-distributed structures, but because of the nature of the upstream disturbances generated in the simulation, such structures would be temporary in nature. They would appear at scattered locations along the span and disappear as the simulation goes on due to the way the upstream disturbances are introduced; hence, their overall effect on the spanwise variation of the mean flow would get smeared out as the statistics are time-averaged, and this could explain the weak variations observed in the skin friction. Once the flow enters the favorable pressure gradient region, the stabilizing effect of the favorable pressure gradient, and also of the convex curvature encountered later in the favorable pressure gradient region, appears to attenuate the spanwise variations. Note that the standard deviation begins to increase again once the flow enters the adverse pressure gradient region past the apex. The surface curvature is still convex there, but as will be seen later, a shear layer begins to form within the decelerating boundary layer. This shear layer generates large-scale structures whose footprint on the near-wall region would cause the behavior in the standard deviation of the skin friction. To reiterate, the flow separates at about  $x/L = 0.1$ . We should also note that the time-averages in the present simulation were taken over  $11L/U_\infty$ . With a much longer time-average, the standard deviations in the skin-friction distributions would likely decrease, although the overall trend with respect to  $x/L$  would likely stay the same. In conclusion, our observations from this analysis seem to largely concur with the previous related observations of Barlow and Johnston [35].

**Evolution of mean streamwise velocity and Reynolds stresses:** We now examine the evolution of the mean streamwise velocity and Reynolds stresses. For this analysis, the mean velocity and Reynolds stress components originally defined in the Cartesian coordinate system are first interpolated from the simulation grid onto the local wall-normal line constructed at a given streamwise station. Using the local wall-normal and surface tangent vectors, the interpolated values are then transformed to the corresponding quantities in the local orthogonal coordinate system. Figure 10 depicts the evolution of the mean streamwise velocity profiles in wall units at several stations. Upstream of the acceleration region, at  $x/L = -0.4$ , we find that the von Kármán constant of  $\kappa = 0.41$  and an intercept constant of  $C = 4.9$  is a good fit to the logarithmic layer of the profile. The upstream flow approaching the foot of the bump first encounters a mild adverse pressure gradient region, which is believed to be responsible for the slightly lower  $C$  value compared to that found in zero pressure gradient turbulent boundary layers. The concave curvature in that region might also have an effect on the logarithmic layer, as discussed further below. The acceleration begins at around  $x/L = -0.29$ . We observe a significant change to the shape of the velocity profiles, as well as to the initial logarithmic layer, as the accelerated flow approaches the apex. The flow visualizations do not show any hint of relaminarization or stabilization at  $Re_L = 2$  million, yet significant changes to the logarithmic layer still do happen. At  $x/L = -0.2$  and  $-0.1$ , we see that part of the velocity profile shifts above the standard logarithmic layer, very much like the observation of Fernholz and Warnack [38] in strongly-accelerated nonrelaminarizing flows.

Some effect of the surface curvature on the law of the wall in the acceleration region is likely. As noted in the review of Patel and Sotiropoulos [39] on the curvature effects in turbulent boundary layers, under negligible streamwise pressure gradient, the velocity profiles on a convex surface lie above the standard logarithmic layer, while those on a concave surface lie below. In our case, the strong favorable pressure gradient overlaps with the concave curvature from  $x/L \approx -0.29$  until  $x/L \approx -0.138$ . The velocity profiles in that region lie above the standard logarithmic layer, which suggests that the favorable pressure gradient effect overwhelms any potential concave surface effect on the law of the wall. The deviation from the logarithmic layer increases in the convex region. By the time the flow reaches and passes the apex, where the adverse pressure gradient takes over, part of the velocity profile shifts back toward the standard logarithmic layer, as seen at the stations of  $x/L = 0$  and  $0.05$ . The curvature is still convex there, but the observed change in

the velocity profile suggests that the adverse pressure gradient effect is stronger than the convex curvature effect on the law of the wall. The flow will soon separate at  $x/L \approx 0.1$ , before the logarithmic layer evolves further.

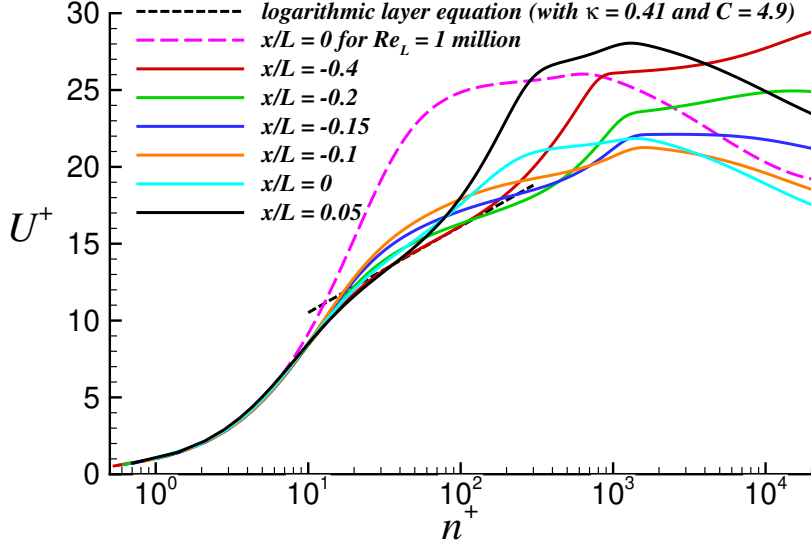


**Figure 10. Mean streamwise velocity profiles in wall units.**

To make a comparison with the previous  $Re_L = 1$  million case, the corresponding apex velocity profile from that case is also shown in Figure 10. The apex profile at  $Re_L = 1$  million, in contrast, looks very much like those of relaminarizing boundary layers observed in laboratory experiments [40]. Therefore, the boundary-layer state at the beginning of the adverse pressure gradient region past the apex is significantly different between the two simulated  $Re_L$  cases; this “initial state” will determine the severity of downstream separation, as discussed further in section 3.2.3.

The evolution of the Reynolds stress components, scaled by  $U_\infty^2$ , from  $x/L = -0.4$  to just upstream of the apex is shown in Figure 11. Here,  $\langle u'u' \rangle$ ,  $\langle v'v' \rangle$ ,  $\langle w'w' \rangle$  and  $\langle u'v' \rangle$ , respectively, are the streamwise, wall-normal, spanwise and shear components of Reynolds stress in the local orthogonal system at a given station, and the  $\langle \rangle$  operator denotes averaging in time and along the span. The wall-normal distance,  $n$ , is normalized by the local  $\delta$ . The first station at  $x/L = -0.4$  is positioned slightly upstream of the acceleration region, while the last station at  $x/L = -0.025$  is close to where the  $C_f$  peak is found. As discussed earlier in Uzun and Malik [7], [8], an internal layer is triggered by the switch from the mild adverse to strong favorable pressure gradient at the foot of the bump, at  $x/L \approx -0.29$ . The formation of this internal layer is signaled by the formation of knee points in the streamwise and spanwise Reynolds stress profiles. The original peaks of the streamwise and spanwise components of the Reynolds stress are already quite close to the wall; thus, they become engulfed within this internal layer, while those of the wall-normal and shear components are located further away from the wall and happen to lie outside this layer. Consequently, we observe that the original peaks in the streamwise and spanwise stress profiles strengthen considerably as the internal layer develops further within the accelerating flow. We also see the emergence of inner peaks in the other two Reynolds stress components within the internal layer in the later stages of the acceleration.

To estimate the thickness of the internal layer generated within the accelerated flow, we employ the method used by Baskaran et al. [4], which is illustrated in Figure 12. This figure shows the total pressure versus the stream function,  $\Psi = \int_0^n U d\eta$ , where  $\eta$  is the variable of integration along the wall-normal

direction, at the apex. As seen in the figure, the rate of change of the total pressure with respect to the stream function is rather fast close to the wall, and slows down further away from the wall. The  $n/\delta$  location where the initial fast rate of change transitions to a relatively slower pace can be taken as the approximate edge of the internal layer. The determination of the internal layer thickness in this matter is admittedly somewhat ambiguous since the precise location where the said rate of change transitions from a fast to a moderate value is usually not clear cut. Nevertheless, the method provides a reasonable method of estimating the internal layer thickness. According to Figure 12, the internal layer thickness scaled by the local  $\delta$  is  $\delta_i/\delta \approx 0.18$  at the apex.

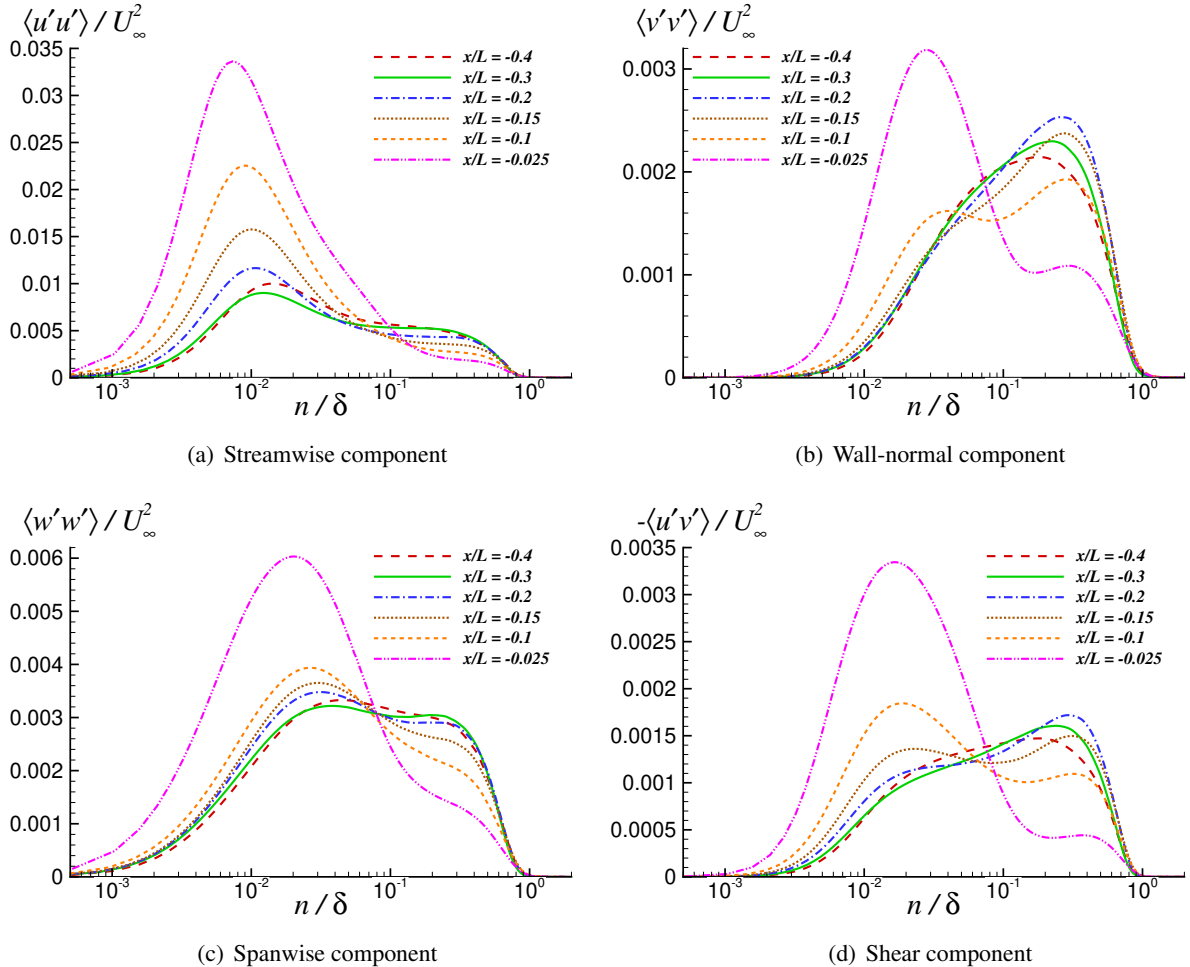


**Figure 11. Evolution of the Reynolds stress profiles.**

Table 1 provides the approximate  $\delta_i/\delta$  values extracted at several streamwise stations in the acceleration region using the described method<sup>‡</sup> and the corresponding values scaled by  $L$ . We see that the the internal layer thickness is initially  $1.1 \times 10^{-3}L$ , and grows to  $2.7 \times 10^{-3}L$  at the apex. The percentage of the local boundary layer covered by the internal layer is 6 percent at the start of the acceleration, and increases to 18 percent at the apex (while the boundary layer thickness decreases in the favorable pressure gradient region).

<sup>‡</sup>A clever algorithm that determines the internal layer thickness using this method can be devised and implemented in a computer program to obtain the  $\delta_i/\delta$  variation over the entire region of interest. This exercise was not attempted in the present study.

This percentage range falls within the typical wall-modeled portion of a boundary layer in a WMLES. The internal layer continues to grow in the deceleration region and occupies about 40 percent of the local boundary layer thickness at the point of separation. As discussed further in section 3.2.3, the upcoming analysis suggests a close connection between the internal layer generated in the upstream region, and the free shear layer that develops in the deceleration region and separates. Therefore, if this inner layer is not modeled correctly, accurate prediction of the downstream smooth body flow separation in this problem may not be feasible in a WMLES.

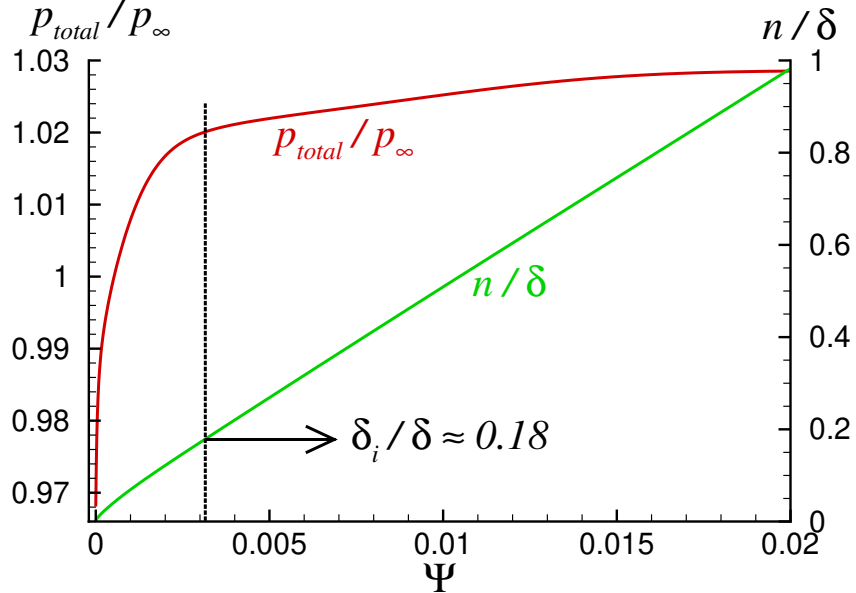


**Figure 12. Total pressure versus the stream function at the bump apex.**

**Table 1. Approximate value of the internal layer thickness at several streamwise locations.**

| $x/L$ | $\delta_i/\delta$ | $\delta_i/L$ |
|-------|-------------------|--------------|
| -0.3  | 0.06              | 0.0011       |
| -0.2  | 0.09              | 0.0017       |
| -0.1  | 0.13              | 0.0021       |
| 0     | 0.18              | 0.0027       |
| 0.05  | 0.24              | 0.0042       |
| 0.1   | 0.4               | 0.0095       |

The steepening near-wall velocity gradient in the wall-normal direction within the accelerating flow is an important ingredient of the near-wall turbulent kinetic energy production, which additionally depends on the existence of the Reynolds shear stress. The production of the Reynolds shear stress, on the other hand, is contingent upon the presence of the gradient of the streamwise velocity in the wall-normal direction and the wall-normal Reynolds stress. The turbulent kinetic energy production mainly takes place in the production term of the streamwise Reynolds stress transport equation, and the fluctuating pressure redistributes the energy from the streamwise stress to the other two normal stresses. The favorable pressure gradient is believed to interfere with that energy redistribution process, and this causes the tendency toward relaminarization/stabilization previously observed in the lower  $Re_L$  case [7], [8]. This interference naturally

impacts what portion of the turbulent kinetic energy gets directed from the streamwise component to the other two normal components. The amount of energy in the wall-normal component then determines the level of Reynolds shear stress production. Hence, there is a mutual dependence between the production of the turbulent kinetic energy and that of the Reynolds shear stress.

Figure 11 also shows that the original outer peaks in the wall-normal and shear stress profiles appear to first strengthen from  $x/L = -0.3$  to  $-0.2$ , before starting to weaken, while the outer levels in the other two components start to decrease monotonically from  $x/L = -0.3$ . We do not have an explanation for this peculiarity. It could be related to the opposing effects of the favorable pressure gradient and the concave curvature on the Reynolds stresses (stabilizing vs. destabilizing, respectively) in the region where those two effects overlap. Deep into the acceleration region, all stress components drop significantly in the outer layer, due to the stabilizing effect of both the favorable pressure gradient as well as the convex curvature, while the internal layer generates the strong near-wall peaks in all components. These strong near-wall peaks can be considered another indication for the lack of relaminarization/stabilization at the present  $Re_L$ . Because of the relaminarization/stabilization in the previous lower  $Re_L$  case, all near-wall stress peaks except that of the streamwise component are much weaker in that case. The flow is able to generate relatively high levels of streamwise stress near the wall in the lower  $Re_L$  case, but the energy transfer to the other normal components becomes hampered by the favorable pressure gradient and the convex curvature, resulting in mixing suppression along the wall-normal and spanwise directions. This mixing suppression also reduces the Reynolds shear stress production.

Figure 13 depicts the variation of the peak values of the Reynolds stress components in the region where  $-0.3 < x/L < 0.1$ , which covers the acceleration region and the early part of adverse pressure gradient region until flow separation. We observe that the peak streamwise component grows remarkably within the internal layer and reaches its maximum value at  $x/L \approx -0.023$ , which is very near the peak  $C_f$  location. The peak streamwise component then starts to decrease as the flow nears the apex and enters the adverse pressure gradient region. This decrease continues until  $x/L \approx 0.066$ , after which the peak streamwise component starts to increase again. As will be seen in section 3.2.3, this is due to the weakening of the inner peak in the early stages of deceleration, and the emergence of an outer streamwise stress peak at the same time. The strength of the outer peak surpasses that of the inner peak starting at about  $x/L = 0.066$ .

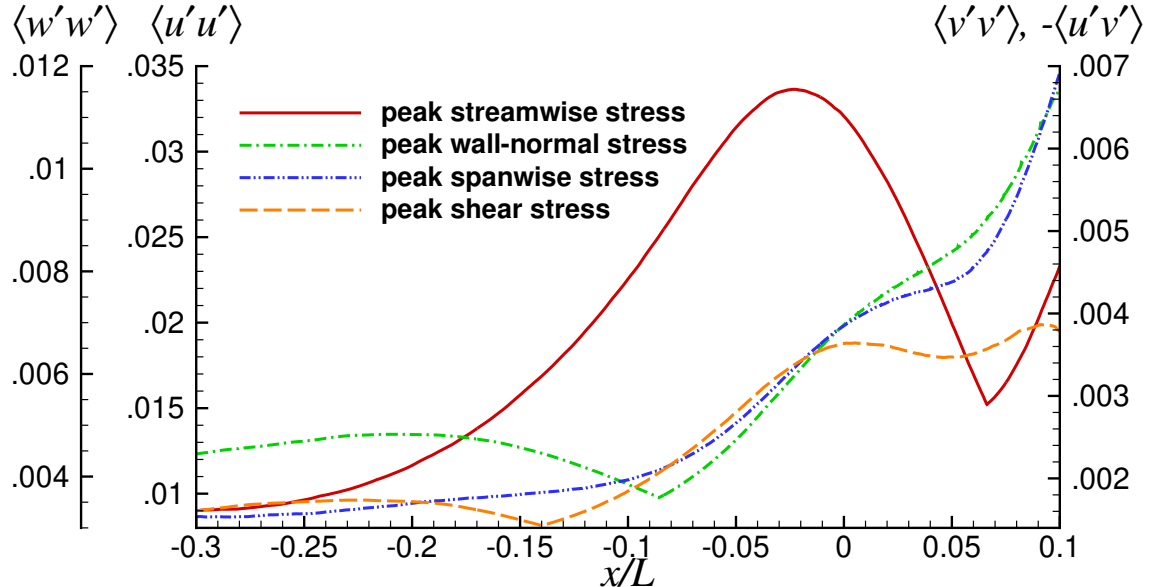


**Figure 13. Variation of the peak values of the Reynolds stress components, scaled by  $U_\infty^2$ .**

We also see in Figure 13 that the strong growth in the peak values of the wall-normal and spanwise stress components starts relatively late in the acceleration region, at about  $x/L \approx -0.08$ , while that in the shear component begins a bit earlier, at about  $x/L = -0.14$ . As observed earlier, the original peaks in the wall-normal and shear components show some growth in the early stages of the flow acceleration. These outer region peak stresses then start to decay while the new inner peaks emerge within the developing internal layer. This is why we find a sudden change in the variation of the peak wall-normal and shear components at  $x/L \approx -0.086$  and  $-0.14$ , respectively, as the inner peak strength surpasses that of the outer peak. As noted above, the accelerated growth in the peaks of the wall-normal and spanwise stress components within the internal layer starts at about  $x/L \approx -0.08$ . There is also a significant rise in the peak streamwise component magnitude by the time the flow reaches  $x/L = -0.08$ ; hence, in the later stages of the acceleration, the buildup in the streamwise stress levels appears to be allowing sufficient energy transfer to the other two normal components that strengthens the near-wall peaks of those components, despite the interference of the favorable pressure gradient with this transfer.

It is also interesting to note that the peak wall-normal and spanwise components display significant growth rates as the flow passes the apex and moves toward separation, while the shear component appears to go through an undulation in that region. At the apex, the streamwise component peak within the internal layer is positioned very close to the wall, at  $n/\delta \approx 0.007$ , while the peaks in the other components are located in the vicinity of  $n/\delta \approx 0.02\text{--}0.03$ . As will be seen in section 3.2.3, the inner peak of the streamwise stress profile weakens in the deceleration region due its close proximity to the wall, and a new outer peak emerges at about the same wall-normal distance to which the inner peaks of the other stress components shift in that region. These peaks happen to be positioned within the shear layer developing in the deceleration region. These observations suggest an inherent link between the internal layer generated in the acceleration region and the emerging shear layer in the deceleration region.

Figure 14 provides the profiles of the anisotropy parameters,  $\langle v'v' \rangle / \langle u'u' \rangle$  and  $\langle w'w' \rangle / \langle u'u' \rangle$ , at the same streamwise stations shown in the Reynolds stress profiles of Figure 11. As expected, we find a high degree of anisotropy within the internal layer identified earlier. This is not surprising at all, given the close proximity to the wall. As seen earlier, the streamwise stress profile contains much of the turbulent kinetic energy in the near-wall region, and the streamwise stress peak within the internal layer is the closest to the wall. There is little, if any, wall-normal stress relative to the streamwise stress in the very near-wall region, say where  $n/\delta < 10^{-2}$  or so, over the entire acceleration region. The ratio between the spanwise and streamwise stress levels in the same very near-wall region drops as the internal layer develops, and appears to start increasing near the apex. The observed downward trend in  $\langle w'w' \rangle / \langle u'u' \rangle$  very near the wall in much of the acceleration region is believed to be a consequence of the favorable pressure gradient interfering with the transfer of the turbulent kinetic energy from the streamwise Reynolds stress to the other two normal components. As noted earlier in the discussion of Figure 13, the energy transfer process appears to be relatively less impeded in the later stages of the acceleration.

Both anisotropy parameter values are generally higher further away from the wall. As the accelerated flow moves toward the apex, we start to see some tendency toward isotropy in the outer region of the boundary layer, roughly corresponding to where  $n/\delta > 0.1\text{--}0.2$ , as indicated by the values exceeding 0.6 in that region. This is believed to be due to the stabilizing effect of a favorable pressure gradient and also of convex streamline curvature in the late stages of acceleration. As the flow nears the apex, a reverse trend back toward anisotropy is observed in the outer region, presumably due to the adverse pressure gradient effect. Note that, as seen in the Reynolds stress profiles, starting at  $n/\delta \approx 0.8$  or so, the stresses become very small near the boundary layer edge. Therefore,  $\langle v'v' \rangle / \langle u'u' \rangle$  exceeds 1, while  $\langle w'w' \rangle / \langle u'u' \rangle$  becomes as high as about 0.8 there. Once the flow enters the favorable pressure gradient downstream of  $x/L = -0.3$ , there is hardly any meaningful collapse of the anisotropy profiles over the portion of the boundary layer containing the bulk of the turbulent kinetic energy, indicating the complexity of the accelerated flow. The anisotropy varies quite significantly not only along the wall-normal direction but also in the streamwise direction.

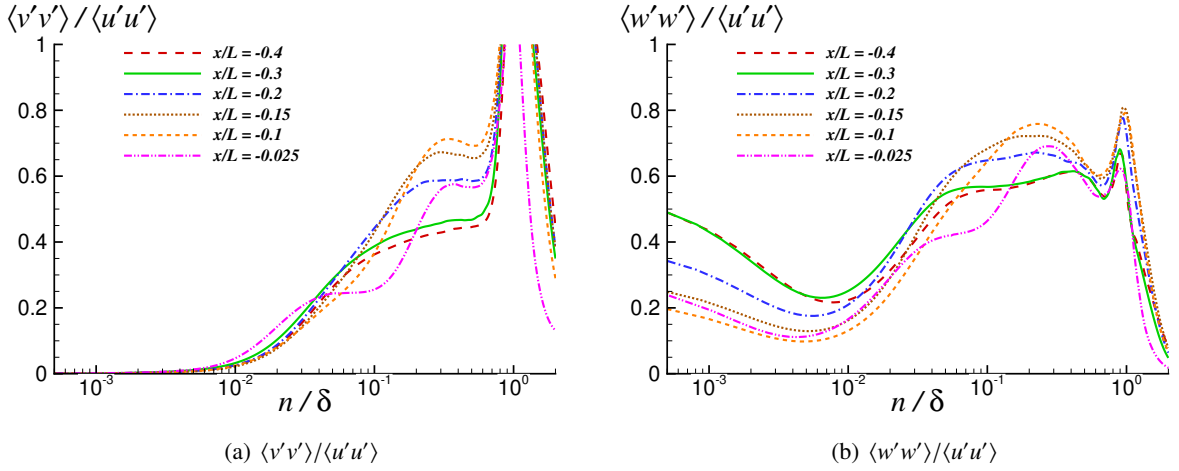


**Figure 14. Anisotropy parameter profiles.**

Figure 15 shows the profiles of the Townsend structure parameter,  $-\langle u'v' \rangle/q^2$ , where  $q^2 = 2k = \langle u'u' \rangle + \langle v'v' \rangle + \langle w'w' \rangle$  ( $k$  is the turbulent kinetic energy), and the streamwise variation of the maximum structure parameter value in the region of interest. Figure 15(a) shows that at  $x/L = -0.4$ , the peak value is nearly constant at around 0.142–0.146 in the range  $0.2 < n/\delta < 0.6$ . This is fairly close to the value of about 0.14 for a zero pressure gradient boundary layer [5]. The stations of  $x/L = -0.3, -0.2$  and  $-0.15$  are located over the concave curvature. The pressure gradient over much of this region is favorable, except at  $x/L = -0.3$ , where it is close to zero. Over the surface distance covered by these stations, the peak portion of the profiles sharpens while gaining strength. Figure 15(b) shows that the station of  $x/L = -0.15$  is very close to where the maximum structure parameter value of 0.194 is found. Recall that the convex curvature begins at  $x/L \approx -0.138$ , which is not too far off from this location. The maximum structure parameter value then starts to decrease as the accelerated flow moves onto the convex curvature. As seen earlier in the discussion of Figure 11, the outer peaks in the wall-normal and shear components of the Reynolds stress show an increase from  $x/L = -0.3$  to  $-0.2$ , before starting to decrease, while the outer levels in the other two components decrease monotonically from  $x/L = -0.3$ . The turbulent kinetic energy in the outer region also decays monotonically in the entire acceleration region. This initial rise in the outer region Reynolds shear stress in combination with the monotonic drop in the turbulent kinetic energy explains the growth of the maximum structure parameter value over the concave surface. The behavior of the peak structure parameter value is reversed in the convex region, suggesting that the rate of decrease in the outer region Reynolds shear stress is faster than that in the turbulent kinetic energy over the convex curvature.

As the flow nears the apex, we see deviations in the structure parameter profiles occurring both near the wall and in the outer regions, relative to the profiles located within the earlier stages of acceleration. As seen in Figure 11(d), an inner Reynolds shear stress peak emerges within the developing internal layer. This shear stress peak corresponds to the inner peak observed at  $x/L = -0.025$  in Figure 15(a). The outer peak in the structure parameter profile weakens as the accelerated flow approaches the apex, which appears to be a consequence of the convex curvature effect according to the preceding analysis. There is also the adverse pressure gradient effect anticipated near the apex, which could explain the significant shape differences observed in the outer region of the structure parameter profiles between the stations of  $x/L = -0.1$  and  $-0.025$ . The strength of the inner peak in the structure parameter profile surpasses that of the outer peak at  $x/L = -0.013$ , which is why the maximum value of the structure parameter in Figure 15(b) begins to rise starting at that location. We also observe that outside the boundary layer at all stations, the structure

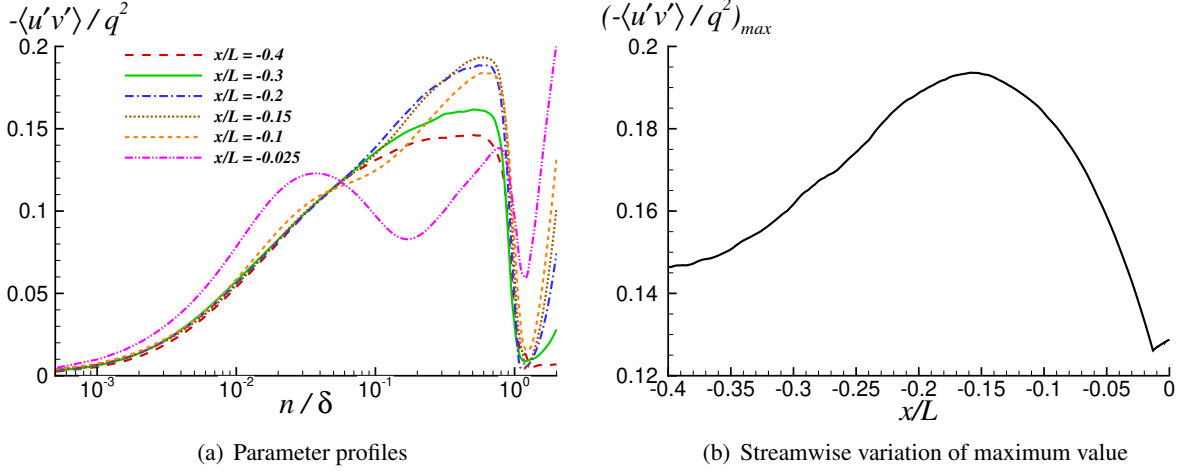


**Figure 15. Townsend structure parameter profiles and variation of maximum value with streamwise distance.**

parameter generally shows an increase with distance from the wall, which suggests that the decay rate of the shear stress with outward distance is slower than that of the turbulent kinetic energy, but the stresses in that region are already very small (see Figure 11); hence, this behavior of the structure parameter outside the boundary layer does not have much practical significance. The other, more relevant observations concerning the evolution of the Townsend structure parameter profiles highlight the subtleties of the Reynolds shear stress behavior relative to the turbulent kinetic energy under the influence of both pressure gradient and surface curvature.

Finally, on a note related to the structure parameter, Bradshaw et al. [41] derived a differential equation for the turbulent shear stress from the turbulent energy equation and defined three empirical functions relating the turbulence intensity, dissipation and diffusion to the shear stress. The equation was solved for various turbulent boundary layers developing under both adverse and favorable pressure conditions, assuming a uniform structure parameter value of 0.15 for all cases. As seen in the above analysis, a uniform structure parameter value across an entire boundary layer subjected to a pressure gradient appears far from a reasonable approximation, and the peak value within the boundary layer can also differ considerably from 0.15, depending on the interaction with the pressure gradient and surface curvature.

### 3.2.3 Examination of the region downstream of the apex

We now move onto the analysis of the decelerating flow past the apex and the downstream reattachment region. As noted earlier, one of the motivations behind the present higher  $Re_L$  simulation is to have a case that generates stronger flow separation in the adverse pressure gradient region, relative to that observed at half the Reynolds number. This is an important feature of the flowfield that will be useful in the evaluation of computationally efficient, lower-fidelity simulation tools. Flow visualizations shown earlier and the  $C_f$  distribution confirmed the presence of more severe separation in the present simulation. A natural question that may arise at this point is: Why does the present higher  $Re_L$  case generate more severe separation relative to that observed at half the Reynolds number? To answer this question, we examine Figures 16(a) and (b) that depict the evolution of the mean streamwise velocity,  $U/U_\infty$ , and the turbulent kinetic energy,  $k/U_\infty^2$ , profiles, respectively, within the deceleration region, for the two simulated cases. The adverse pressure gradient slows down both the near-wall and outer regions of the boundary layer, and this leads to the

formation of an intermediate buffer zone that acts like a free shear layer. In the lower  $Re_L$  case, the partially relaminarized/stabilized flow retransitions to turbulence shortly after the apex, as discussed in Refs. [7], [8]. The velocity profiles shown in Figure 16(a) reveal that the retrransition in the lower  $Re_L$  case generates some near-wall momentum, which then seems to counteract the near-wall deceleration due to the adverse pressure gradient. We therefore see in Figure 16(a) that the initial near-wall deceleration is not as strong as that in the higher  $Re_L$  case. This “supplemental” near-wall momentum creates resistance against separation. The retrransition generates the high peak in  $k$  at  $x/L = 0.05$  in the lower  $Re_L$  case.

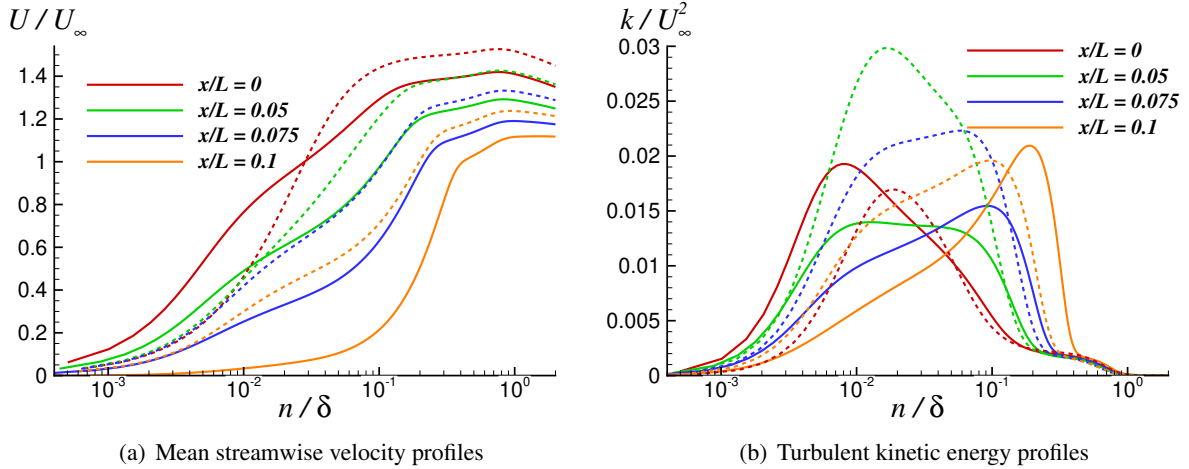


**Figure 16. Comparison of profiles between the two simulated cases. Solid lines correspond to  $Re_L = 2$  million, dashed lines correspond to  $Re_L = 1$  million.**

For the higher  $Re_L$  case, the shape changes in the velocity profiles, coupled with the outward shift in the peak  $k$  location, and the accompanying growth in the peak  $k$ , suggest that the shear layer develops quickly. In that case, the free shear layer spreads wide as the flow reaches  $x/L = 0.1$ ; subsequently, the near-wall momentum nearly vanishes and this will soon lead to separation. For the lower  $Re_L$  case, the shear layer development is relatively slower, due to the supplemental initial near-wall momentum from the retrransition. As the flow moves deeper into the adverse pressure gradient, the peak  $k$  decreases, coupled with an outward shift of the peak  $k$  location into the developing shear layer. The peak  $k$  level in the shear layer will begin to rise shortly after  $x/L = 0.1$ , and the flow will eventually undergo very weak/incipient separation over the range where  $0.195 \lesssim x/L \lesssim 0.268$ . The adverse pressure gradient magnitude in that region is relatively milder compared to that right after the apex, which then causes very weak or incipient separation. Such differences in the shear layer evolution between the two cases, and the severity of separation, are intrinsically tied to the Reynolds number dependent initial states at the entrance of the adverse pressure gradient region past the apex.

Figures 17 and 18 depict how the Reynolds stress profiles develop in the region downstream of the apex for the  $Re_L = 2$  million flow. For clarity, the region of interest is divided into two halves. We find some interesting trends in the evolution of the Reynolds stress profiles. At the apex, the streamwise component peak within the internal layer is positioned very close to the wall, at  $n/\delta \approx 0.007$ , while the peaks in the other components are located in the vicinity of  $n/\delta \approx 0.02$ – $0.03$ . We see a weakening of the streamwise component peak as the flow decelerates toward separation, while the other component peaks begin to shift outward into the emerging shear layer. An outer peak also develops in the streamwise stress profile as the flow decelerates. The weakening of the inner stress peak is due to the reduction in the near-wall streamwise

velocity gradient by the adverse pressure gradient, which then reduces the streamwise stress production. The peaks in the other stress components, initially positioned relatively further from the wall, shift outward without weakening in the deceleration region from  $x/L = 0$  to 0.1. In fact, the wall-normal and spanwise component peaks display a growth. As the flow reaches  $x/L = 0.1$ , which is very near the separation point, all stress peaks are positioned at  $n/\delta \approx 0.2$ . These observations suggest a close connection between the internal layer that develops upstream within the acceleration region, and the free shear layer that emerges in the deceleration region, as also observed previously in the  $Re_L = 1$  million simulation [7], [8]. As noted earlier in section 3.2.2, the percentage of the local boundary layer occupied by the internal layer grows from 6 to 18 percent in the acceleration region. This percentage range falls within the typical wall-modeled portion of a boundary layer in a WMLES. The internal layer continues to grow in the deceleration region and covers about 40 percent of the local boundary layer thickness at the point of separation. Thus, proper physical modeling of this inner layer appears crucial in order for a WMLES to predict the flow separation in this problem.

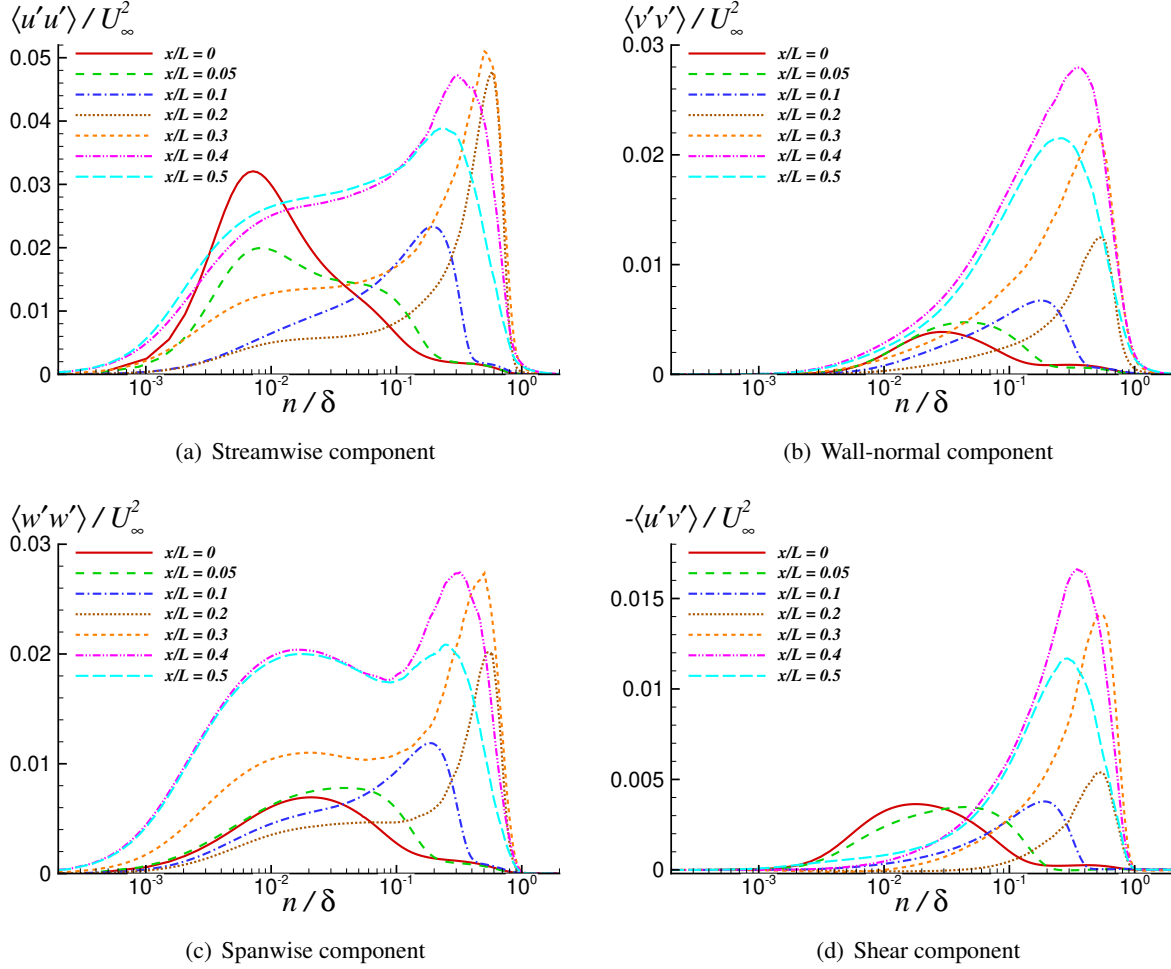


**Figure 17. Evolution of the Reynolds stress profiles in the region where  $0 \leq x/L \leq 0.5$ .**

All stress peaks are positioned at approximately the same location within the separated shear layer. The peak stress location moves away from the wall, denoted by the increasing  $n/\delta$ , as the separated shear layer

evolves, and then moves back toward the wall once the separated flow nears the reattachment location at  $x/L = 0.42$ . All stress peaks show major growth within the separated shear layer. From  $x/L = 0.1$  to 0.2, the peaks of the normal components increase by as much as a factor of 2, while the shear component peak displays a more moderate growth. From  $x/L = 0.2$  to 0.3, a different trend is found; the shear component peak now has the fastest growth with a factor of about 2.6, the wall-normal component peak still shows a fairly significant growth with a factor of about 1.8, while a more moderate growth is found in the spanwise component peak along with the least growth in the streamwise component peak. As the separated shear layer approaches  $x/L = 0.4$ , which is near the reattachment point at  $x/L = 0.42$ , the peak streamwise component has already started to decrease, while the peak spanwise component holds steady, and the other two component peaks are still rising.

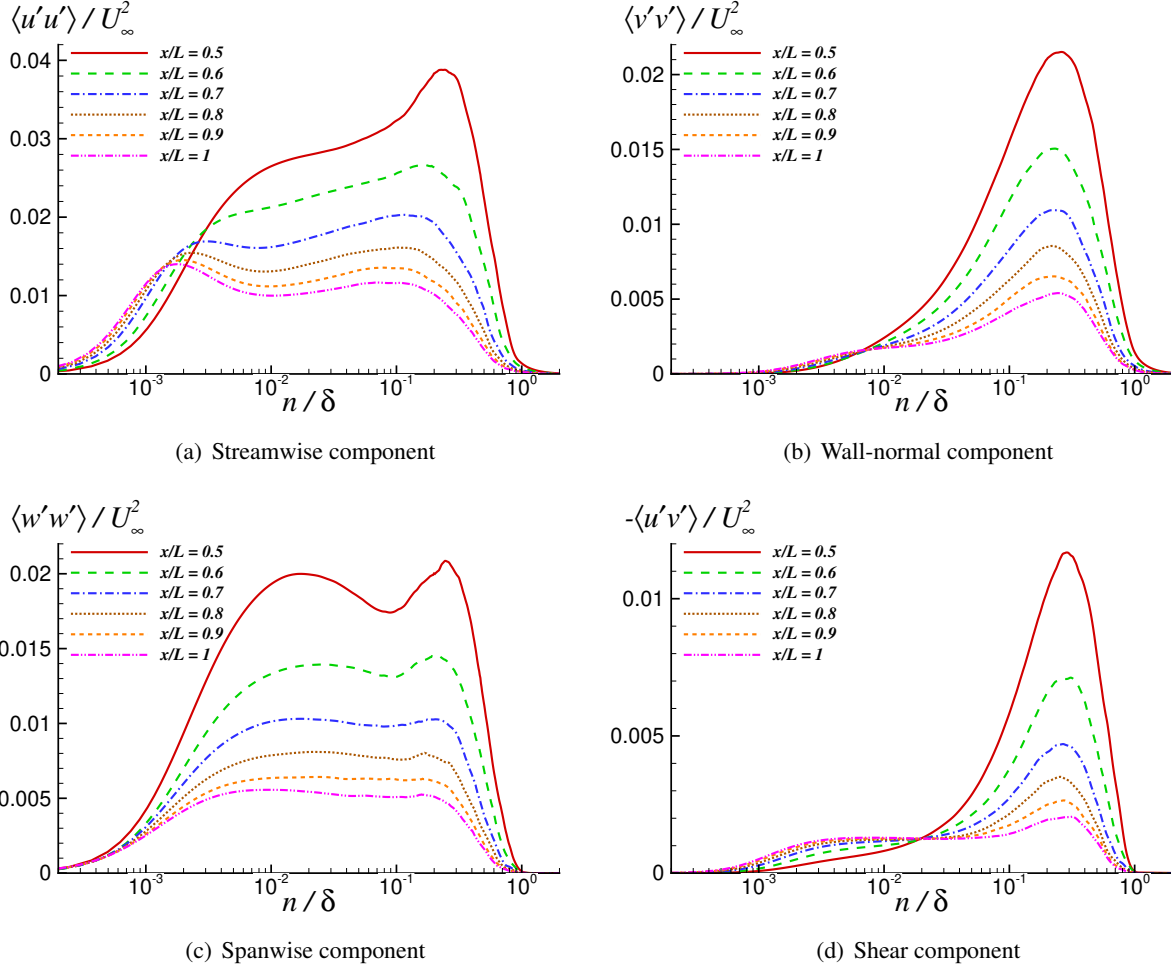


**Figure 18. Evolution of the Reynolds stress profiles in the region where  $0.5 \leq x/L \leq 1$ .**

Another observation we make from Figure 17 is the appearance of considerable streamwise and spanwise stress levels within the reversed flow region as the reattachment point is approached. The separated shear layer generates some energetic eddies that impinge on the wall in the vicinity of the reattachment point. Some of these eddies get diverted into the reversed flow region and move upstream along the wall. Consequently, high levels of streamwise and spanwise Reynolds stresses are found near the reattachment

point. These levels drop as the distance from the reattachment point increases within the reversed flow region because the near-wall eddies slow down as they move further upstream. There is a small rise in the other two stress components in the reversed flow region near the wall as well, but those increases are not as significant, as the wall-normal velocity fluctuations are rather small close to the wall.

The energetic eddies of the shear layer impinging on the wall that do not get diverted into the reversed flow region end up getting dragged downstream by the reattached flow. This is why we also observe significant near-wall levels in the streamwise and spanwise stresses at  $x/L = 0.5$ , which is located downstream of the reattachment point. These near-wall eddies getting dragged downstream along the wall begin to lose their coherence, which then reduces the associated near-wall stress levels. At the same time, we also observe the formation of a new inner streamwise Reynolds stress peak very near the wall, which is an indication of a new internal layer being generated within the recovery flow. This internal layer is believed to be triggered by the change from adverse to mild favorable pressure gradient at the tail of the bump. The other Reynolds stress components are also in the process of generating their respective inner peaks. As our physical domain ends at  $x/L = 1$ , there is not sufficient development length for the inner peak to complete its development in the Reynolds stress profiles. Meanwhile, the peak stresses found in the shear layer above the wall have started decaying within the recovering flow. The shear layer gradually disappears as the velocity gradient within the free shear layer is progressively decreased by the mild favorable pressure gradient in the recovery region. This naturally decreases the Reynolds stress production there. With a longer recovery domain length, the outer peaks in all Reynolds stresses would completely disappear, and the inner peaks would complete their development. We would then expect the Reynolds stress profile shapes to approach those of a fully developed turbulent boundary layer under zero or mild favorable pressure gradient conditions.

#### 4 Concluding remarks

The findings from a high-fidelity simulation of a narrow slice of the speed bump flow at  $Re_L = 2$  million show that the higher Reynolds number flow generates much stronger flow separation, relative to that previously observed at half the Reynolds number. The present higher  $Re_L$  is also able to suppress the relaminarization/stabilization in the acceleration region observed at the lower  $Re_L$ . An internal layer is found to develop within the accelerated flow, which is believed to be triggered by the switch from the mild adverse to strong favorable pressure gradient at the foot of the bump. Strong peaks in all Reynolds stress components emerge as this internal layer continues its development within the favorable pressure gradient region. The acceleration region of the flow displays strong anisotropy in the normal Reynolds stress profiles. The anisotropy varies quite significantly not only along the wall-normal direction but also in the streamwise direction. Both pressure gradient and surface curvature effects are responsible for the trends observed in the evolution of the anisotropy profiles. Not surprisingly, there is a high degree of anisotropy within the internal layer. Toward the apex, there is a tendency toward isotropy in the outer region of the boundary layer, believed to be due to the stabilizing effect of favorable pressure gradient and also of convex streamline curvature in the late stages of acceleration. The ratio between the Reynolds shear stress and the turbulent kinetic energy goes through significant changes via the interaction with the pressure gradient and surface curvature related effects as well. Analysis of the concave curvature section upstream of the apex did not reveal a significant spanwise variation in the time-averaged skin-friction distributions, which, in turn, can be considered evidence for the lack of organized stationary structures over the concave surface.

Comparison of the present  $Re_L = 2$  million results with the previous  $Re_L = 1$  millions results revealed that the Reynolds number dependent boundary-layer state at the entrance of the adverse pressure gradient region past the apex dictates the severity of separation. In the  $Re_L = 2$  million case, the turbulent boundary layer past the apex starts immediately decelerating and separates at about  $x/L = 0.1$ , while in the  $Re_L = 1$  million case, the partially relaminarized/stabilized boundary layer at the apex first goes through a retran-

sition to turbulence in the early stages of the adverse pressure gradient. This retransition generates some supplemental near-wall momentum that creates resistance against separation. Subsequently, the lower  $Re_L$  flow undergoes very weak or incipient separation further downstream, where the adverse pressure gradient is relatively milder compared to that immediately after the apex.

The evolution of the Reynolds stress profiles within the decelerating, separated and reattached portions of the flow displayed dramatic changes as the flow went through these stages. The analysis suggests a strong connection between the internal layer generated in the upstream region, and the free shear layer that develops in the deceleration region and separates. Therefore, if this inner layer is not modeled correctly, accurate prediction of the downstream smooth body flow separation may not be possible. In any case, the quality dataset generated by the present simulation provides a valuable resource for evaluating lower-fidelity simulation tools applied to turbulent flows that develop under curvature and strong pressure gradient effects and experience smooth-body separation.

## Acknowledgments

This work was sponsored by the NASA Transformational Tools and Technologies Project of the Transformative Aeronautics Concepts Program under the Aeronautics Research Mission Directorate. The calculations were made possible by the computing resources provided by the NASA High-End Computing Program through the NASA Advanced Supercomputing Division at Ames Research Center. The RANS solution for the mean inflow conditions was provided by Dr. Prahladh Iyer.

## References

- [1] Slotnick, J. P., Integrated CFD Validation Experiments for Prediction of Turbulent Separated Flows for Subsonic Transport Aircraft, NATO Science and Technology Organization, Meeting Proceedings RDP, STO-MP-AVT-307, 2019.
- [2] Williams, O., Samuell, M., Sarwas, S., Robbins, M. and Ferrante, A., Experimental Study of a CFD Validation Test Case for Turbulent Separated Flows, AIAA Paper 2020-0092, AIAA SciTech 2020 Forum, Orlando, Florida, 2020.
- [3] Williams, O., Samuell, M., Robbins, M. L., Annamalai, H. and Ferrante, A., Characterization of Separated Flowfield over Gaussian Speed-Bump CFD Validation Geometry, AIAA Paper 2021-1671, AIAA SciTech 2021 Forum, Virtual Event, 2021.
- [4] Baskaran, V., Smits, A. J. and Joubert, P. N., A Turbulent Flow over a Curved Hill Part 1. Growth of an Internal Boundary Layer, *Journal of Fluid Mechanics*, 1987, 182, 47–83.
- [5] Webster, D. R., DeGraff, D. B. and Eaton, J. K., Turbulence Characteristics of a Boundary Layer over a Two-Dimensional Bump, *Journal of Fluid Mechanics*, 1996, 320, 53–69.
- [6] Greenblatt, D., Paschal, K. B., Yao, C.-S., Harris, J., Schaeffler, N. W. and Washburn, A. E., A Separation Control CFD Validation Test Case, Part 1: Baseline and Steady Suction, *AIAA Journal*, 2006, 44(12), 2820–2830.
- [7] Uzun, A. and Malik, M. R., Simulation of a Turbulent Flow Subjected to Favorable and Adverse Pressure Gradients, AIAA Paper 2020-3061, AIAA Aviation 2020 Forum, Virtual Event, 2020.
- [8] Uzun, A. and Malik, M. R., Simulation of a Turbulent Flow Subjected to Favorable and Adverse Pressure Gradients, *Theoretical and Computational Fluid Dynamics*, Published online: 02 March 2021.

- [9] Balin, R., Jansen, K. E. and Spalart, P. R., Wall-Modeled LES of Flow over a Gaussian Bump with Strong Pressure Gradients and Separation, AIAA Paper 2020-3012, AIAA Aviation 2020 Forum, Virtual Event, 2020.
- [10] Iyer, P. S. and Malik, M. R., Wall-modeled LES of flow over a Gaussian bump, AIAA Paper 2021-1438, AIAA SciTech 2021 Forum, Virtual Event, 2021.
- [11] Wright, J. R., Balin, R., Evans, J. A. and Jansen, K. E., Unstructured LES<sub>DNS</sub> of a Turbulent Boundary Layer over a Gaussian Bump, AIAA Paper 2021-1746, AIAA SciTech 2021 Forum, Virtual Event, 2021.
- [12] Uzun, A. and Malik, M. R., Large-Eddy Simulation of Flow over a Wall-Mounted Hump with Separation and Reattachment, *AIAA Journal*, 2018, 56(2), 715–730.
- [13] Uzun, A. and Malik, M. R., Wall-Resolved Large-Eddy Simulations of Transonic Shock-Induced Flow Separation, *AIAA Journal*, 2019, 57(5), 1955–1972.
- [14] Ashcroft, G. and Zhang, X., Optimized Prefactored Compact Schemes, *Journal of Computational Physics*, 2003, 190(2), 459–477.
- [15] Lele, S. K., Compact Finite Difference Schemes with Spectral-like Resolution, *Journal of Computational Physics*, 1992, 103(1), 16–42.
- [16] Gaitonde, D. V. and Visbal, M. R., Padé-Type Higher-Order Boundary Filters for the Navier-Stokes Equations, *AIAA Journal*, 2000, 38(11), 2103–2112.
- [17] Visbal, M. R. and Gaitonde, D. V., Very High-Order Spatially Implicit Schemes for Computational Acoustics on Curvilinear Meshes, *Journal of Computational Acoustics*, 2001, 9(4), 1259–1286.
- [18] Ekaterinaris, J. A., Implicit, High-Resolution, Compact Schemes for Gas Dynamics and Aeroacoustics, *Journal of Computational Physics*, 1999, 156(2), 272–299.
- [19] Uzun, A., Hussaini, M. Y. and Streett, C. L., Large-Eddy Simulation of a Wing Tip Vortex on Overset Grids, *AIAA Journal*, 2006, 44(6), 1229–1242.
- [20] Uzun, A. and Hussaini, M. Y., Investigation of High Frequency Noise Generation in the Near-Nozzle Region of a Jet Using Large Eddy Simulation, *Theoretical and Computational Fluid Dynamics*, 2007, 21(4), 291–321.
- [21] Uzun, A. and Hussaini, M. Y., Simulation of Noise Generation in Near-Nozzle Region of a Chevron Nozzle Jet, *AIAA Journal*, 2009, 47(8), 1793–1810.
- [22] Uzun, A. and Hussaini, M. Y., Prediction of Noise Generated by a Round Nozzle Jet Flow Using Computational Aeroacoustics, *Journal of Computational Acoustics*, 2011, 19(3), 291–316.
- [23] Uzun, A. and Malik, M. R., Effect of Spatial Filtering in Implicit Large-Eddy Simulations of Separated Flows, *AIAA Journal*, 2019, 57(12), 5575–5581.
- [24] Spalart, P. R. and Garbaruk, A. V., Correction to the Spalart-Allmaras Turbulence Model, Providing More Accurate Skin Friction, *AIAA Journal*, 2020, 58(5), 1903–1905.
- [25] Schlatter, P. and Örlü, R., Assessment of Direct Numerical Simulation Data of Turbulent Boundary Layers, *Journal of Fluid Mechanics*, 2010, 659, 116–126.

- [26] Spalart, P. R. and Watmuff, J. H., Experimental and Numerical Study of a Turbulent Boundary Layer with Pressure Gradients, *Journal of Fluid Mechanics*, 1993, 249, 337–371.
- [27] Badri Narayanan, M. A. and Ramjee, V., On the Criteria for Reverse Transition in a Two-Dimensional Boundary Layer Flow, *Journal of Fluid Mechanics*, 1969, 35(2), 225–241.
- [28] Narasimha, R. and Sreenivasan, K. R., Relaminarization in Highly Accelerated Turbulent Boundary Layers, *Journal of Fluid Mechanics*, 1973, 61(3), 417–447.
- [29] Spalart, P. R., Numerical Study of Sink-Flow Boundary Layers, *Journal of Fluid Mechanics*, 1986, 172, 307–328.
- [30] Patel, V. C. and Head, M. R., Reversion of Turbulent to Laminar Flow, *Journal of Fluid Mechanics*, 1968, 34(2), 371–392.
- [31] So, R. M. C. and Mellor, G. L., Experiment on Convex Curvature Effects in Turbulent Boundary Layers, *Journal of Fluid Mechanics*, 1973, 60(1), 43–62.
- [32] Muck, K. C., Hoffmann, P. H. and Bradshaw, P., The Effect of Convex Surface Curvature on Turbulent Boundary Layers, *Journal of Fluid Mechanics*, 1985, 161, 347–369.
- [33] So, R. M. C. and Mellor, G. L., Experiment on Turbulent Boundary Layers on a Concave Wall, *Aeronautical Quarterly*, 1975, 26(1), 25–40.
- [34] Hoffmann, P. H., Muck, K. C. and Bradshaw, P., The Effect of Concave Surface Curvature on Turbulent Boundary Layers, *Journal of Fluid Mechanics*, 1985, 161, 371–403.
- [35] Barlow, R. S. and Johnston, J. P., Structure of a Turbulent Boundary Layer on a Concave Surface, *Journal of Fluid Mechanics*, 1988, 191, 137–176.
- [36] Saric, W. S., Görtler Vortices, *Annual Review of Fluid Mechanics*, 1994, 26, 379–409.
- [37] Morgan, B., Larsson, J., Kawai, S. and Lele, S. K., Improving Low-Frequency Characteristics of Recycling/Rescaling Inflow Turbulence Generation, *AIAA Journal*, 2011, 49(3), 582–597.
- [38] Fernholz, H. H. and Warnack, D., The Effects of a Favourable Pressure Gradient and of the Reynolds Number on an Incompressible Axisymmetric Turbulent Boundary Layer. Part 1. The Turbulent Boundary Layer, *Journal of Fluid Mechanics*, 1998, 359, 329–356.
- [39] Patel, V. C. and Sotiropoulos, F., Longitudinal Curvature Effects in Turbulent Boundary Layers, *Progress in Aerospace Sciences*, 1997, 33(1–2), 1–70.
- [40] Warnack, D. and Fernholz, H. H., The Effects of a Favourable Pressure Gradient and of the Reynolds Number on an Incompressible Axisymmetric Turbulent Boundary Layer. Part 2. The Boundary Layer with Relaminarization, *Journal of Fluid Mechanics*, 1998, 359, 357–381.
- [41] Bradshaw, P., Ferris, D. H. and Atwell, N. P., Calculation of Boundary-Layer Development using the Turbulent Energy Equation, *Journal of Fluid Mechanics*, 1967, 28(3), 593–616.

**REPORT DOCUMENTATION PAGE**Form Approved  
OMB No. 0704-0188

The public reporting burden for this collection of information is estimated to average 1 hour per response, including the time for reviewing instructions, searching existing data sources, gathering and maintaining the data needed, and completing and reviewing the collection of information. Send comments regarding this burden estimate or any other aspect of this collection of information, including suggestions for reducing the burden, to Department of Defense, Washington Headquarters Services, Directorate for Information Operations and Reports (0704-0188), 1215 Jefferson Davis Highway, Suite 1204, Arlington, VA 22202-4302. Respondents should be aware that notwithstanding any other provision of law, no person shall be subject to any penalty for failing to comply with a collection of information if it does not display a currently valid OMB control number.

**PLEASE DO NOT RETURN YOUR FORM TO THE ABOVE ADDRESS.**

|  |  |  |  |                                  |
|--|--|--|--|----------------------------------|
| 1. REPORT DATE (DD-MM-YYYY)<br>01/05/2021  | 2. REPORT TYPE<br>TECHNICAL MEMORANDUM | 3. DATES COVERED (From - To)                                       |  |                                  |
| 4. TITLE AND SUBTITLE<br><br>High-Fidelity Simulation of Turbulent Flow Past a Gaussian Bump   |  |  | 5a. CONTRACT NUMBER  |                                  |
|  |  |  | 5b. GRANT NUMBER   |                                  |
|  |  |  | 5c. PROGRAM ELEMENT NUMBER                                       |                                  |
| 6. AUTHOR(S)<br>Ali Uzun, Mujeeb R. Malik  |  |  | 5d. PROJECT NUMBER   |                                  |
|  |  |  | 5e. TASK NUMBER  |                                  |
|  |  |  | 5f. WORK UNIT NUMBER<br>109492.02.07.05.01.01                    |                                  |
| 7. PERFORMING ORGANIZATION NAME(S) AND ADDRESS(ES)<br><br>NASA Langley Research Center<br>Hampton, VA 23681-2199   |  |  | 8. PERFORMING ORGANIZATION<br>REPORT NUMBER                      |                                  |
| 9. SPONSORING/MONITORING AGENCY NAME(S) AND ADDRESS(ES)<br><br>National Aeronautics and Space Administration<br>Washington, DC 20546-001   |  |  | 10. SPONSOR/MONITOR'S ACRONYM(S)<br>NASA                         |                                  |
|  |  |  | 11. SPONSOR/MONITOR'S REPORT<br>NUMBER(S)<br>NASA/TM-20210013648 |                                  |
| 12. DISTRIBUTION/AVAILABILITY STATEMENT<br><br>Unclassified - Unlimited<br>Subject Category<br>Availability: NASA STI Program (757) 864-9658   |  |  |  |                                  |
| 13. SUPPLEMENTARY NOTES  |  |  |  |                                  |
| 14. ABSTRACT<br><br>A spanwise-periodic computation of a turbulent flow past a Gaussian bump is performed in the form of a hybrid direct numerical simulation and wall-resolved large-eddy simulation. A fourth-order spatially-accurate flow solver is employed to perform the simulation, using 10.2 billion grid points for a Reynolds number of 170000 based on the bump height. The key findings from the simulation are reported in the acceleration and deceleration flow regions associated with the bump shape. |  |  |  |                                  |
| 15. SUBJECT TERMS<br><br>Turbulent Boundary Layer, Pressure Gradient, Flow Separation, Surface Curvature   |  |  |  |                                  |
| 16. SECURITY CLASSIFICATION OF:<br><br>a. REPORT<br>U  |  | b. ABSTRACT<br>U   | c. THIS PAGE<br>U  | 17. LIMITATION OF ABSTRACT<br>UU |
| 18. NUMBER OF PAGES<br>36  |  | 19a. NAME OF RESPONSIBLE PERSON<br>HQ - STI-infodesk@mail.nasa.gov |  |                                  |
|  |  | 19b. TELEPHONE NUMBER (Include area code)<br>757-864-9658          |  |                                  |